Grant agreement no. 312818
SPA.2012.2.2-01 : Key technologies enabling observations in and from space

- Collaborative project -

WP 1 - Scientific definition of Instrument Requirements

D1.3
Satellite position requirements
and preliminary stability assessment

Due date of deliverable: month 25
Actual submission date:
Start date of project: January 1st 2013   Duration: 36 months

Lead beneficiary for this deliverable: CNRS - LAM
Last editor: K. Dohlen, Laboratoire d'Astrophysique de Marseille (CNRS-LAM)

Contributors:
V. Iafolla (AGI), G. Savini (UCL), S. Vives (CNRS-LAM), E. Pascale (Cardif)

Project co-funded by the European Commission within the Seventh Framework Programme (2007-2013)		
Dissemination Level (please refer to the list of deliverables in Annex 1 and complete also footer)		
PU	Public	■
PP	Restricted to other programme participants (including the Commission Services)	
RE	Restricted to a group specified by the consortium (including the Commission Services)	
CO	Confidential, only for members of the consortium (including the Commission Services)	

HISTORY TABLE

Version	Date	Released by	Comments
Draft00	23/9/14	KDo	Original skeleton
Draft02	25/11/14	VIa	First draft
Draft08	9/2/15	LAM-CNRS	Final draft

TABLE OF CONTENTS

1 INTRODUCTION

1.1 OBJECTIVES

This document concerns two main issues: satellite position and pointing. The objectives of the document are defined in the FISICA DOW as:

"Satellite position requirements and preliminary stability assessment: Stemming from the scientific products identified this document will highlight the desired tolerances in satellite position and stability as well as mirror tolerances."

Please note that all aspects concerning mirror tolerances are actually described in another deliverable (D1.2) and will therefore not be treated in the present document.

1.2 STUDY CONTEXT

For knowledge to progress in many aspects of astrophysics it is clear that we need to make observations at all wavelengths that at least match the spatial resolution achieved in the optical by the Hubble Space Telescope. This is especially true in the Far Infra-Red (FIR) waveband, covering the 30-300 micron region where our atmosphere is opaque, for which the necessity of space borne experiments makes achieving high spatial resolution particularly difficult, see Figure 1. At present, FIR observations lie in a resolution gap of 2 orders of magnitude represented by the James-Webb Space telescope in the mid-infrared on one side and the ALMA interferometer on the other. Only with the development of space borne interferometers can we hope to bridge this divide.

Several studies of space-based interferometers have been made during the last 20 years. These can be divided into two main groups, optical and thermal infrared interferometers for exoplanet research, mainly based on nulling in order to search for or study faint circumstellar objects (Darwin, TPG, Pegasus, …), and more versatile observatories for high-resolution imaging in the far infrared (FIRI, SPECS, …). While the former requires extreme (nanometric) precision and stability in terms of absolute optical path difference adjustment in order to reach the required high-contrast nulling performance, the latter essentially only needs to satisfy the $\lambda/4$ criterion for optical path difference (OPD) control, taking the precision requirement up to some 10 μm, in order to satisfy the imaging criterion.

The number of telescopes varies from study to study. While basic nulling can be achieved with two telescopes (Pegase), constraints imposed by the non-zero angular extent of nearby stars indicates the use of four or more collectors (Darwin, SIM, …). While imaging can be achieved with two telescopes, providing single instantaneous baseline observation (SPECS, …), the use of several collectors increase the observing efficiency by the multiplication of baselines and provides the advantage of phase closure, further relaxing OPD control requirements (FIRI-CV).

The number of individual space-craft units is also highly variable from one proposal to another. In short-baseline proposals, providing typically decametric baselines, telescopes can be mounted together on a beam structure, leading to a single space-craft design. Hectometric baselines can be achieved using tethers (Lorenzini) or free-flying concepts (Darwin, FIRI-CV…), while kilometric designs would probably only be possible using free

flyers (FIRI-CV). While tethers physically connect telescopes to each-other, this connection is not structural, and individual units will need to be fully-fledged satellites with their own power, communication, attitude control, etc. In the case of heterodyne interferometers, in which a local oscillator provides a common phase reference for each telescope as implemented in radio telescopes, the number of space crafts equals the number of telescope. In the case of homodyne (or direct detection) interferometers, the technique developed for optical interferometry (VLTI) where heterodyning is not possible, an additional beam-combiner spacecraft. This added complexity is offset by the increased sensitivity offered by this technique which can operate at much lower spectral resolutions than the Heterodyne system.

The science case studies effectuated during the first year of the FISICA study (D1.1, Spinoglio et al) concluded that a maximum baseline of 100m would be required to provide a compelling scientific output from such an instrument. While this baseline dimension is easily compatible with tether designs (Lorenzini), we consider in this document the possibility of implementing a structural boom design for this baseline, possibly offering a more conservative and less risky design than tethers in terms of interferometer navigation and pointing.

While we also consider free-flying option for completeness, it is clear that the generally accepted view is that this technique is highly risky, in spite of encouraging results from the PRISMA mission and current investments into the Proba-3 solar observation mission.
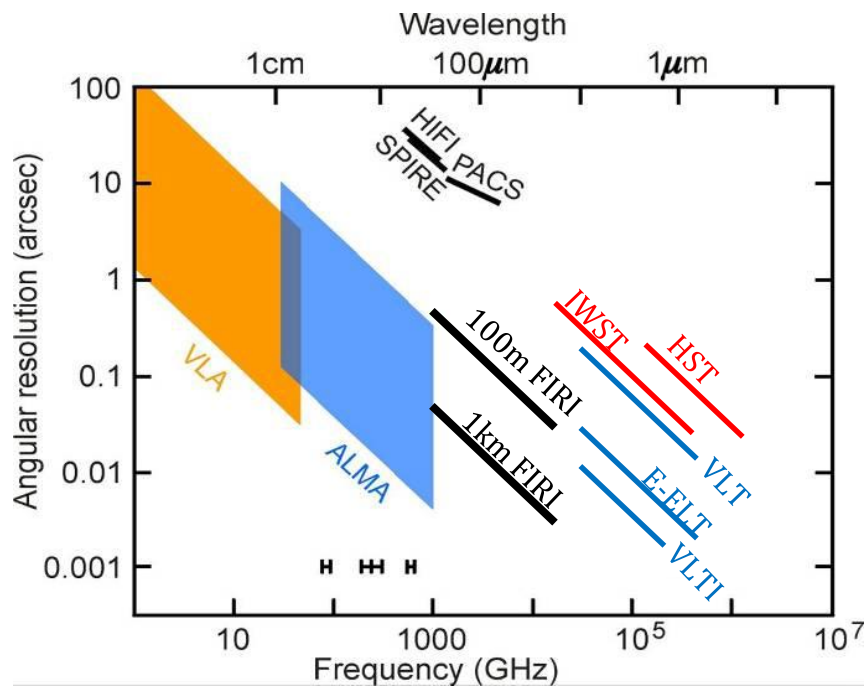
Figure 1. A gap in spatial resolution is seen between capabilities offered by existing (VLT, VLTI, HST) and upcoming (JWST, E-ELT) facilities in the optical below 10-20 microns and large millimeter and radio observatories (ALMA, VLA). While these facilities offer sub-arcsecond resolution, observations in the far-infrared, from 30 to 300 microns aer limited to the 10-100 arcsecond performance offered by the instruments (SPIRE, HIFI, PACS) flown on the Herschel space observatory. Resolution offered by 100m and 1km Far infrared space interferometers is indicated.

1.3 TOP-LEVEL REQUIREMENTS APPLICABLE TO THIS DOCUMENT

Mission requirements are discussed in the following documents:

D1.1: Science requirements

D1.2: Instrument performance requirements preliminary document

The latter document formulates specific requirements, of which the following are applicable to the present document:

R2.1.1. The continuous spectral coverage for the instrument will be from 25 to 400µm.

R2.2.2. The baseline will be variable from a few metres up to a maximum inter-telescope distance of 100m.

R3.5.1. The absolute pointing error will have a requirement of <2 arcsec RMS and a goal of <1 arcsec.

R3.5.2. A tracking accuracy of <1 arcsec RMS will be maintained over a 24 hr period (typical observing period) with a goal of <0.5 arcsec.

ACKNOWLEDGEMENTS

DISCLAIMER

The content of this deliverable does not reflect the official opinion of the European Union. Responsibility for the information and views expressed in the deliverable therein lies entirely with the author(s).

ACRONYMOUS

AOCS Attitude and Orbit Control System

APE Actual Pointing Error

Arcmin Arc minute. 1 arcmin = 1/60 degrees

Arcsec Arc second. 1 arcsecond = 1/60 arcmin = 1/3600 degrees

BC Beam Combiner

CoM Centere of mass

DoF Degree of Freedom

FD/FDS Flight Dynamics/Flight Dynamics System

FFT Fast Fourrier Transforms

FIR Far Infra-Red

FIRI Far InfraRed Interferometer

FSU Fringe Sensor Unit

FTS Fourier Transform Spectrometer

G/S Ground Station

H/W Hardware

HGA High Gain Antenna

HK HouseKeeping data

IFOV Interferometric Field Of View

ILS Instrument Line Shape

IR Infrared

ISL Inter-satellite link
ISO Infrared Space Observatory
ITD Inter-Telescope Distance
L2 Second Lagrangian Equilibrium Point (Sun-Earth System)
MGA Medium Gain Antenna
MM Mass Memory
NEP Noise Equivalent Power
NER Noise Equivalent Radiance
OBC On-Board Computer
OBT On-Board Time
ODL Optical Delay Line
OPD Optical Path Difference
PLM Payload Module
RMS Root Mean Square
RW Reaction wheel
S/C Spacecraft
S/W Software
SA Solar Array
SADM Solar Array Drive Mechanism
SNR Signal to Noise Ratio
SRP Solar radiation pressure
SSEA Sun-Spacecraft-Earth Angle
TBC To Be Confirmed
TBD To Be Defined
TC Telecommand
TM Telemetry
WFE Wave Front Error

2 GENERAL CONCERNS FOR A SPACE-BASED INTERFEROMETER

The analysis here reported is connected to the task_1.3 "Identify key satellite requirements" of the FISICA (Far Infrared Space Interferometer Critical Assessment). One of the main parts of this task is the identification of the requirements for the satellites in terms of vibrational noise that can be tolerated, requirements on the AOCS in order to satisfy the science objective and to identify algorithms necessary to maintain satellite positions during the scientific observations. In this subsection a simple analysis of the concept for a space double Fourier interferometer, FIRI like or SPECS interferometer, is reported considering as primary scope the clarification of the concept regarding the perturbing action of noise presents on the elements of the space interferometer.
The material is organized in the following parts:
- Basic concept for a double Fourier Interferometer
- Analysis of the possible missions and ideas for a Space Infrared Interferometer Telescope

Other specific issues analysed in more details in the successive subsections are:
- Analysis of the possible influence of the vibrational noise presents on the single satellite and on their constellation, related to the interferometric measurements.
- Requirements on the level of vibrational noise that can be tolerated.

2.1 HISTORICAL FRAMEWORK

Large ground-based telescopes currently achieve sub-arc-second resolution observations in the visible and near infrared spectrum using 10-m class telescopes. To reach such resolutions at longer infrared wavelengths, the laws of diffraction imposes the use of 100m or even 1km sized structures. The FISICA study is a direct consequence of the strong recommendation to the scientific community for the development of space optical and infrared astronomy that was indicated in the 2000 Decadal Report "Astronomy and Astrophysics in the New Millennium". For the infrared, a far-IR *kilometer baseline* interferometer, known as SPECS (Submillimeter Probe of the Evolution of Cosmic Structure) was studied as a NASA "vision mission" in its Science Plan for astrophysics. The 2003 the Community Plan for Far-IR/Submillimeter Space Astronomy recommended SPIRIT, a *structurally-connected* interferometer, as a practical step toward to the more ambitious SPECS mission.
Following these study, in the October 2004 the ESA AWG (Astronomy Working Group) of the Science Directorate, recommended a study of a far infrared interferometer mission (FIRI), in preparation of the Cosmic Vision program. This kind of mission could be the natural successor for a higher-resolution European far-infrared telescope after Herschel.

2.2 CONCEPT STUDIES

As base reference for the work here presented are considered the three studies before cited:
- SPECS: kilometric baselines
- SPIRIT: decametric baseline

- FIRI-ESA: decametric baseline

These three mission concepts consider an assembly of two telescopes separated from a common hub collector by a means permitting to vary the inter-telescope distance or baseline, mechanically or by free-flying navigation. The considerations made in the following concerning the base concepts of work for a FIR mission and noise level tolerate on the satellite system are general and can be retained for all these systems. In the Table 1 is reported a list of the main measurement requirements for SPECS, FIRI and SPIRIT

Table 1. Requirements for three typical concepts for a future FIR mission.

Measurement Requirements	SPECS	SPIRIT	FIRI
Wavelength range (μm)	40-640	25 – 400	25-300
Instantaneous FoV (arcmin)	1	1	1
Angular Resolution (arcsec)	0.02 @ 100 μm	0.5 @ 100 μm	0.25 @ 30 μm; 2.5 @ 300 μm
Spectral Resolution ($\Delta\lambda/\lambda$)	3000	3000	3000
Point Source Sensitivity (5σ, 24 hours)		Spectral line: $10^{-19} W\ m^{-2}$ Continuum: 10 μJy	
Science Time per Field		24 hours	24 h
Field of Regard	40° band centered on ecliptic	40° band centered on ecliptic	
Max Baseline (m)	1000	36	25
Min Baseline	As short as possible	As short as possible	As short as possible

2.2.1 SPIFFY concept

In order to provide a realistic and timely contribution to the study of a space-based FIR interferometer, the present study concentrates on a moderate concept referred to as SPIFFY. In Figure 2 and in the two following tables are reported the configuration and the principal parameters considered in the trade-off analysis performed in the FISICA study, concerning the medium ground between the minimal baseline and the over-ambitious kilometric baseline.
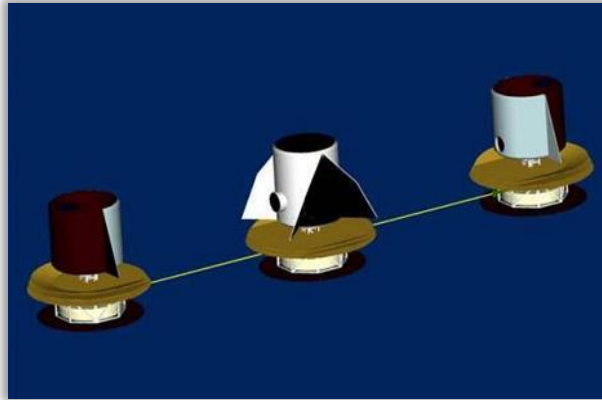
Figure 2. SPIFFY configuration, a medium ground between the minimum baseline and ambitious formation flying baseline

Table 2. Main characteristics for the SPIFFY configuration

Instrument Characteristics		
Primary diameter	2 m	ext
Baseline Range	0, 10-100m	ext
Optics Temperature	4K cryo-cooled	([1])
Configuration	Rigid Truss or Tether	([3])
Mission Lifetime	3-5Yrs	ext
Sky Coverage	+/- 20 deg. from ecliptic	([1,2])
Spectral Coverage (μm)	25-50,50-100,100-200,200-400	([1])
Detector Arrays (35/70/140/280μm)	2x(28x28/14x14/8x8/4x4)	([*])

Table 3. Derived parameters for the SPIFFY configuration

Angular resolution	0.1 (lambda/100um) arcsec	([1])
Field of View	1 arcminute	([1,3])
Spectral resolution	~3000-5000	([1])ext.
Point Source Sensitivity (5s in 24hrs) -) Spectral Line (10^{-19} W/m^2) -) Continuum (μJy)	(35 / 70 / 140 / 280) μm 0.7 / 0.4 / 0.3 / 0.3 3.5 / 5 / 7.5 / 12	Ext.
Typical Observation Time	1 day	([1])

(*) *Sensitivity ext. on primary scaling only. Detector numbers are scaled to maintain f.o.v. size.*

The SPIFFY concept originates from a merging of the ambitious concept for SPECS with a "scaled up" version of the SPIRIT concept and a logarithmic middle ground between the latter and the ESA FIRI cosmic vision proposal concept formation flying configuration. While this concept is listed in order to allow a middle ground between a rigid short baseline boom interferometer and the ambitious formation flying, it does assume technical solutions which are less defined than either of the other concepts.

In the technology trade-off presented here, we consider the options of structurally connected telescopes, tether connection, and free-flyers.

In the preliminary works with which the scientific requirements are translated into a requirements for the measurements, the following questions are taken into account:

  ➢ Is high-fidelity imaging required?
  ➢ Which are the highest priorities in wavelength coverage?

➢ What kind of spectral resolution throughout the available bands is of interest?
➢ Is there a Time-Transient nature to the observation?
➢ Is an instantaneous field of view of 1 square arcmin sufficient?
➢ Is the field of regard constraint a major limitation for the proposed science?

2.3 BASIC CONCEPT FOR A DOUBLE FOURIER INTERFEROMETER

In this subsection an idea of the basic concept of a space interferometer will be given, to perform the combined (DFM) double Fourier modulation so to obtain the spatial image of the source for all its spectral components in the required wavelength range.

In the proposed FIR space telescope, SPECS, SPIRIT and FIRI, a single scientific instrument gives the possibility to combine spatial and spectroscopic measurements at the same time, making use of a Michelson stellar interferometer with a scanning optical delay line for Fourier transform spectroscopy. In this architecture, light from the two telescopes is combined at the pupil plane and the combined signal is detected by means of detector focal plane arrays. In particular their two telescopes can move to operate at many interferometric baselines, permitting to resolve several spatial structure with the necessary angular scales, so to produce high quality far-IR images. The maximum image resolution is determined by the maximum baseline length of the apparatus. In order to obtain very high sensitivity, otherwise limited by astrophysical background photon noise, the principal optical elements of the interferometers are cooled to (or below) 4 K and high sensitive detectors (at sub-K temperatures) are used.

As mentioned, to obtain simultaneously both the image of an area of sky and its emission spectrum, an interferometric technique, suggested originally by Mariotti and Ridgway (1988), that combines interferometry for images, with the spectrometric interferometry by means of Fourier transforms was considered

Two telescopes placed at a distance B between them, pointed precisely at the same area of the sky, the collected light is recombined, after entering on one of the two beams a phase temporal delay. The combination of the two beams can be sent to a single-pixel detector and the signal acquisition, made in function of the delay, is the interferogram, whose Fourier transform gives the frequency spectrum of the sources in the area of sky observed. The amplitude of each observed frequency or corresponding wavelength, is the amplitude of the harmonic component associated with sources of wavelength λ, separated by an angle equal to

$$\alpha = \frac{\lambda}{2B}$$

for sources aligned with the baseline of the interferometer B, in that specific elementary step of measurement (point of the plane u, v).

If a detailed image is desired with this technique, it is necessary for the u-v plane to be densely sampled by making measurements with the interferometer in all possible positions obtained by changing the distance between the two telescopes both in radial position (Bmin to Bmax) and orienting the baseline in all angular positions. If the telescopes have a diameter of $1m$, the maximum non-redundant uv-sampling is obtained by moving them (both radial and angular) with steps of the order of $0.5\ m$.

2.3.1   Spatial Interferometry

To obtain an image of a sky area is necessary to perform for every single point of the u, v plane the spectrographic interferometry. Every single point (u, v), acquired by the interferometer, gives the spatial Fourier component for a fixed distance between the sources contained in the sky area in observation and in a direction parallel to the telescope baseline and for the various spectroscopic components.

The Van Cittert-Zernike theorem indicates the possibility to obtaining a good approximation of the distribution of the sources, even if the u, v plane has not been completely filled.

2.3.2   Spectrographic Interferometry

To perform the spectrographic interferometry, the combination of the two beams coming from the two telescopes, can be sent to a single-pixel detector and this acquisition, made as a function of the delay, is the interferogram, whose Fourier transform gives the spectral frequency of the source.
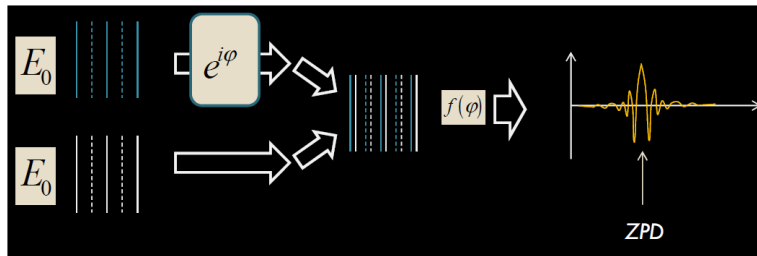
Assuming that the delay is introduced by varying the optical path of one of the two beams by means of an optical delay line that moves with constant speed v, making an acquisition of the signal intensity in function of time with an acquisition time equal to Δt, and then the spectral analysis of this signal, we will be able to see a maximum frequency determined by the acquisition time (Nyquist theorem), equal to:

$$f_{max} = 1/(2 \cdot \Delta t)$$

which corresponds to the minimum wavelength detectable (maximum spatial frequency), given by the relation:

$$\lambda_{min} = v/f_{max} = 2 \cdot \Delta t \cdot v$$

The max measurement period T, will correspond to the minimum detectable frequency, equal to

$$f_{min} = \frac{1}{T}$$

The maximum wavelength to which the instrument is sensitive will be equal to the maximum optical path difference which can be in turn expressed through the period T necessary to scan it (at speed v).

$$\lambda_{max} = \Lambda = v \cdot T$$

If we want a spectral resolution equal to R:

$$R = \frac{\lambda}{\Delta \lambda} = \frac{v \cdot T}{2 \cdot \Delta t \cdot v} = \frac{T}{2 \cdot \Delta t}$$

The resolution is determined by the ratio between the duration time of the scan and the double of the sampling time.

In summary:

• The maximum wavelength is given by the maximum optical path difference introduced (maximum distance made by the slide);

• The spatial frequency of the maximum or the minimum detectable wavelength is given by the Nyquist frequency and then by the spatial sampling (distance made by the slide between an acquisition and the other).

2.4 SYSTEM GENERAL CHARACTERISTICS

2.4.1 General description of the interferometer

In Figure_3.4.2_1 a basic concept configuration for a Far InfraRed Interferometer telescope is shown, while in Figure_3.4.2_2 the concept of the optical configuration is shown.
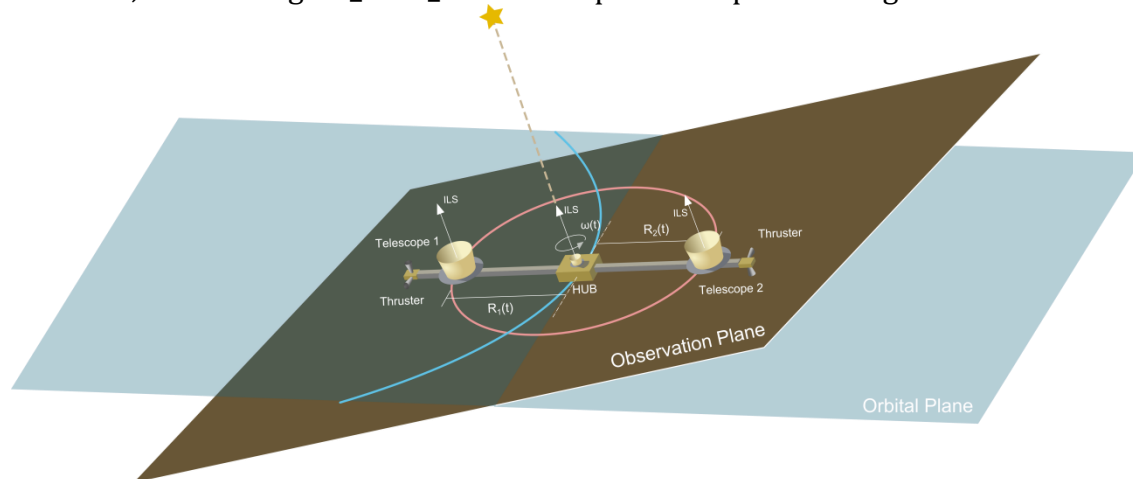
Figure_3.4.2_1 *Base-line configuration of a Far Infrared Interferometer telescope*
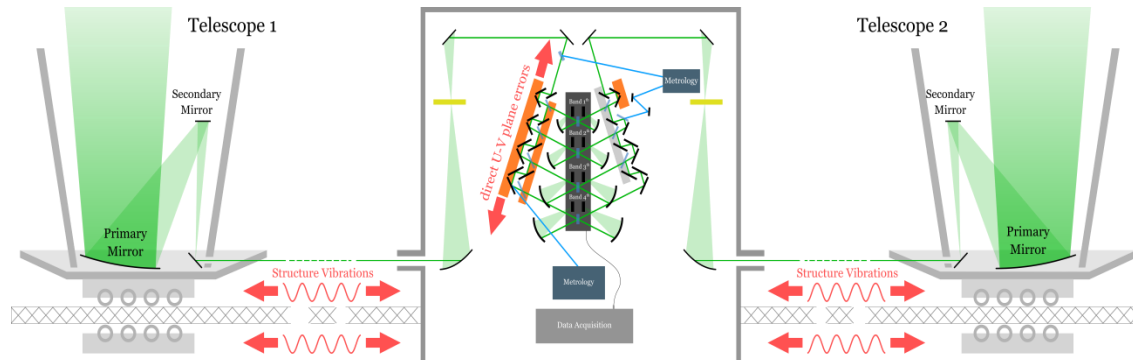
Figure_3.4.2_2 *Optical configuration: the light collected by the two telescopes is sent to the beam combiner at 4K, the optical delay line mechanism splits the beams into four wavelength band and introduces a delay in one of them, before sending them to the detectors - figure modified from Leisawitz (2007) .*

To obtain simultaneously both the image of an area of the sky and its emission spectrum, a single device is adopted that makes use of the interferometric technique, as suggested by Mariotti and Ridgway (1988), combining spatial interferometry, with the spectrometric interferometry by means of a double Fourier transform.

2.4.2   General context

For a space-based interferometer employing Double Fourier Modulation, knowledge of the propagation of phase errors is essential as well as knowledge of their provenance.

While a detailed design of the instrument would allow specific instrument non-idealities to be associated with deviations from the ideal instrument behaviour (or performance) we can at least categorize a few generic effects and their causes which can be foreseen given known satellite issues.

2.4.3   Baseline configuration and dependencies of collimated beam

The baseline configuration combines two collimated beams originating from the two satellites employing independent pointing control systems.
Pointing errors come in different forms and their implications on the phase variations will be similarly different.
The following definitions are accepted in the community as typical pointing errors [1]:

* [AKE] Absolute Knowledge Error:
* [APE] Absolute Performance Error:
* [KDE] Knowledge Drift Error;
* [KRE] Knowledge Reproducibility Error
* [MKE] Mean Knowledge Error;
* [MPE] Mean Performance Error;
* [PDE] Performance Drift Error;
* [PRE] Performance Reproducibility Error;
* [RKE] Relative Knowledge Error;
* [RPE] Relative Performance Error;

The definitions of these quantities and their inter-relation are remanded to [1].
Specifically the "Performance Errors" are related to the difference between the intended and achieved pointing while the "Knowledge Errors" focus on the difference between the assumed and actual pointing. "Mean" and "Relative" errors are in reference to a given time interval and the finer portion of the error with respect to the same interval. For the purpose of this discussion we will focus on the "Absolute Errors" and their effect on visibility.

Implications of such errors vary with their specific time dependence although this will not be addressed with "Mean" and "Relative" as in the accepted terminology due to the specific use in the instrument of modulation frequencies and Nyquist sampling.

For the causes of noises and pointing variations see the specific sections of the document and Table 8.3 of [1] for additional canonical terms. We can however generalize the errors induced by the specific cause and categorize the effects occurring on the beams and their phases at the beam combiner.

Another two important category boundaries to be considered are the following time quantities. Let us assume that a spectrometer scan is performed in a time T_S with minimum movement from the baseline (i.e. the single spectral scan is considered co-located in the uv-plane) [2]. A second time constant can be considered well distinct from T_S and that is the time relative to the spectrometer fast-scanning optical path sampling Δt which is constrained on the low side (fast) by the detector time constant τ, and on the high side (slow) by the mechanical optical speed "v" of the spectrometer and by baseline movements, all ultimately driven by the overall time taken to perform the measurement.

These two intervals define the ranges of effects (noise or pointing jitter), which will have different effects and repercussions on the data taken.

2.4.4 Phase error budgeting and fringe visibillity

All the elements discussed hereafter will impact the fringe visibility or the interferogram reconstruction. Depending on the allocation of the error budget allowed for this (similarly to an overall optical efficiency goal) one will find that at the end of the study on the nature of the errors we are presented with an exercise to allocate such a budget.

2.5 PHASE ERRORS INDUCED

2.5.1 Optics induced phase error

The optical system will comprise of a number of telescope mirrors, a hub window, relay optics with a cold Lyot stop, the cold-optics mirrors, a set of dichroics, the delay line and ultimately (from an interferometric point of view) the beam combiner before re-imaging optics to focus at the focal plane.

A detailed design of the optics is necessary to produce an optical modelling sufficiently detailed to show how the phase surface presents itself at the beam combiner surface (BCS), which in the ideal case finds the matched phase from the second arm of the interferometer. We can however present here detailed examples of what can be expected for a variety of different effects and how these affect the visibility of a given pixel.
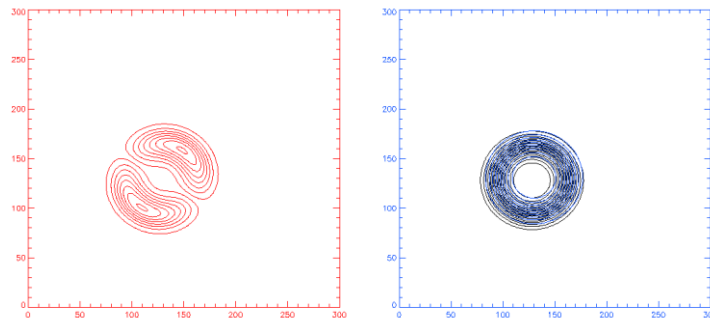
Figure 3. Right: Example of superposition of contour phase map of two beams one of which is shifted due to mirror mis-alignment. Left: Resulting phase difference between two beams.

Surface defects, alignment errors and positioning variations induced by thermal contraction will induce a phase change of some kind which will generate a phase mis-match of the two beams at the BCS (Left Figure 3). The amplitude of the difference shown as an example in Figure 3 has been purposely left with no specific amplitude as the nature of the optical defect (or mis-alignment) will drive its amplitude.

Independently of the cause, the phase errors can be divided into two groups:

1) Optical path difference (OPD). This represents the average phase difference between the two average values of the phase surfaces or simply the average value of the phase difference. Denoted as ξ_i, where i identifies the cause of that particular effect.

2) Wavefront difference (WFD). This represents the relative, zero average, difference between the interfering wavefronts. Denoted as $\psi_i(x,y)$, a map of the phase difference for a specific optical component i.

The OPD will effectively add to the displacement of the instrument Zero Path Difference (ZPD) while the second will impact the overall visibility of the interference fringe. Fringe visibility can be calculated by performing the integral over the cosine of the phase difference $\psi_i(x,y)$.

It is important to note that these effects will be specific for each given input angle in the beam and should hence be modelled separately for a number of different angles.

The portion of the fringe visibility loss budget reserved to optical imperfections will likely impact requirements on the ultimate surface quality and alignment of optical elements.
The following subsections outline some potential effects and suggest a way in which these can be categorized and dealt with. The numerical natures of most of these will depend on a detailed optical design so are difficult to specify exactly. However, some constraints can be placed given the expected performance of the instrument.

2.5.1.1 Optics mis-alignment

One obvious first example is the potential for one of the optical mirrors to suffer from a constant mis-alignment with respect to the nominal optical design. Consequences of this again will depend on which optical element is subject to mis-alignment, the mis-alignment rotation axis and the amplitude of rotation. Similar arguments can be made for mis-position.
The OPD part of such errors is not of great concern as it is constant in time and merely adds to the overall phase delay of one of the two arms of the interferometer. The WFD, $\psi_{i-malign}(x,y)$, on the other hand, would constitute an issue.
In our original error budget (and given the numbers of likely mirrors of the system) we assume that 2% of the visibility is the tolerable limit of error induced by the phase difference across the BCS for the combined effects of optical mis-alignments.

2.5.1.2 BSM tilting

A similar effect but which is factored in the initial optical design of the instrument is the Beam-Steering-Mirror (BSM), likely conveniently placed after each telescope, acting thanks to a tip-tilt mechanism to contain any high-frequency drift of the beams in the sky.
In this subsection we do not refer to pointing issues (next section), but mainly to small changes in the beam and phase surface induced by the change in positions of the BSM. Again, OPD errors will likely be negligible . For WFD we reserve an additional 1% of the visibility error budget.

The reduced budget compared to factual mis-alignments of any fixed mirrors is tied to the non-stationary nature of the BSM which is in theory continuously correcting for any pointing error (or jitter) of the spacecraft. It is foreseen that a likely analysis technique would have to monitor the BSM attitude and potentially correct the fringe visibility for this, depending on the final magnitude of the effect.

2.5.1.3 *Secondary mirror focusing mechanism*

The presence of a focusing mechanism placed at the secondary mirror to allow re-focusing of the telescope once commissioned is a feature of a number of space observatories due to the potential for the telescope to become de-focused after launch. The causes of this could be sought in launch vibrations or more commonly from deviations from the predicted thermal contractions of the entire spacecraft structure. As a result, in order to improve telescope focus, a push-pull broom system can be installed to allow re-focusing of the telescope after commissioning. This feature by itself does not introduce any phase (fringe visibility) error and so is not accounted for as an additional term in the error budget.

2.5.1.4 *Mirror Surface Form Errors*

Given the presence of 7 to 20 mirrors in the path of the incident photons depending on the channel and their different role in the optics chain, a specific term cannot be associated here for a given mirror. We can however point out that all mirrors can be considered "paired" in the two arms of the interferometer and that any deviation between two "paired" mirrors (again other than a full offset term) will produce some visibility reduction. It is fair to point out that space qualified mirrors for these wavelengths are not considered challenging to manufacture.

2.5.2 By proposing a requirement to present a form error of less than $\lambda/16$ in average over the entire surface of any mirror, one could ensure that the difference between the surface of any pair is within twice that and statistically these would compensate when accounting for the relevant phase shifts maintain visibility reduction to a minimum. For telescope mirror requirements in detail see (D1.2). Pointing and AOCS errors

In the specific case of two-beam interferometers, three types of pointing errors must be considered, reflecting the three main elements of the interferometer, each telescope and the baseline joining them.

1) Baseline pointing error: The object at the centre of the FOV is not located in the direction of the normal to the baseline.
2) Common pointing errors where the axis of the two telescopes have a synchronized movement during observation.
3) Differential pointing error which denotes the difference in the pointing between the two telescopes.

A baseline pointing error produces an effective baseline reduction equal to the cosine of the error angle and, more importantly, an error in the optical path difference of the baseline multiplied by the sine of the pointing error. If the interferometer's rotation axis

corresponds to the baseline pointing axis, then this will create a modulation of the OPD. OPD errors can be corrected a posteriori if they are known, so the real issue here is the error of the *knowledge* of the baseline pointing direction. Considering modal calculations of the interferometer structure and using data from the BSM pointing correction, it is likely that pointing related OPD errors can be recovered and used for such a posteriori correction.

A common pointing error is equivalent to a change in the "beam-weighting" of the sky and produces a small amplitude modulation of the sources given their specific position.
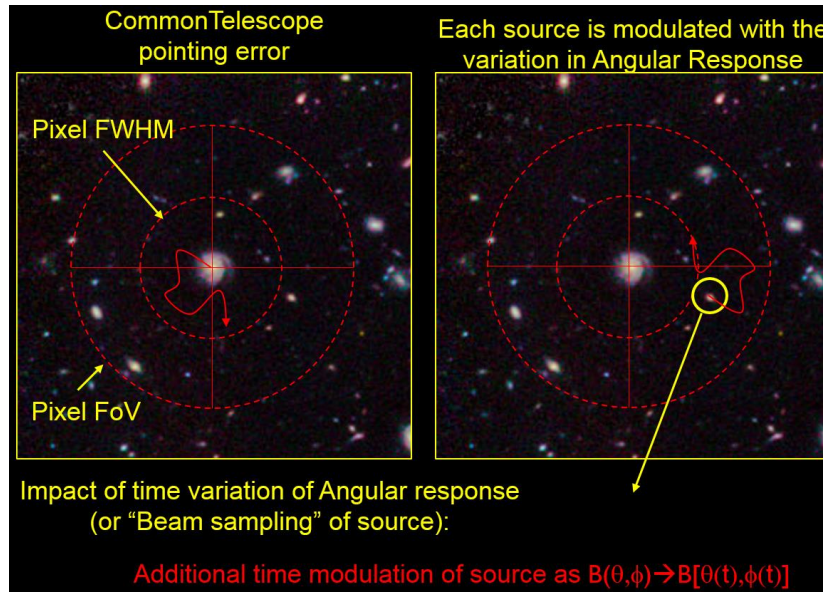
Fig.X. Pointing error as a function of time can be inverted as an amplitude modulation of all the sources in the sky given their position.

Assuming that one would want to maintain such modulation contained to a small fraction of the observed signal, we can suggest for example that such modulation be kept within 5%. The implications of this requirement is that throughout the duration of the observation the local variations of the angular response be kept within that amount.

For a Gaussian beam (assumed only for the purpose of this estimation) pixel FoV of 3.15" @25µm that implies a pointing control requirement of 0.1" (See Figure 4). While 5% may seem quite a relaxed requirement, this effect is reduced as a function of wavelength to be ~1% or less in bands 3 and 4.
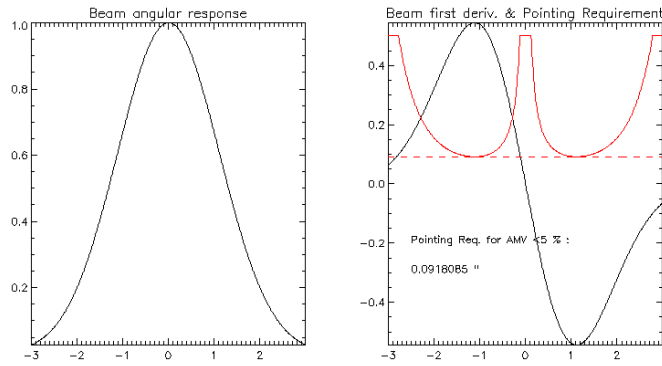
Figure 4. Imposing for the derivative of the beam to be maintained within a certain amplitude. The overall constraint for sources within the beam is for the pointing to be stable within ~0.1". If the 5% seems excessive, one should keep in mind that this is true for the short wavelengths side of band and scales with wavelength becoming less stringent at longer wavelength. Moreover such AMV (Amplitude Modulation Value) is greater at the highest point of the beam derivative – its FWHM – when most of the time the source will be pointed at in the main part of the beam where the requirement is substantially reduced. (The red curve is "maxed" at 0.5" for visual reasons only).

Concerning the differential pointing error, providing this effect is contained within the single pixel FoV for each channel, it will result in a small difference in amplitude of the two components to be combined effectively producing an "imbalance" of the interferometer arms. The effect is then for each source (depending on their position) to split contributions to the interference fringe and to a non-interfering offset, leading to a loss of contrast, see Figure 6.
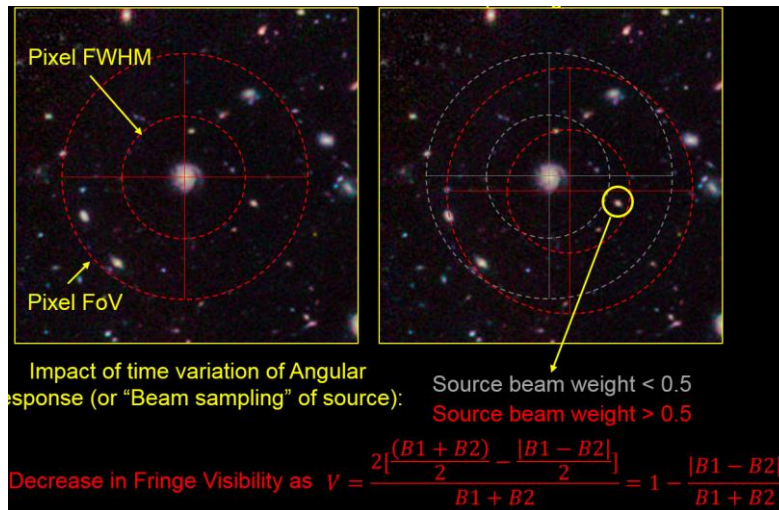
Figure 5. Differential Pointing Error (DPE) is the time dependent difference of the pointing of the two telescopes. The consequence is a small modulation of the fringe visibility (different for each source depending on their position within the beam and the beam differential pointing time variation. Pointing requirements for this term can be imposed similarly to the previous case (with a different effect on the final data).
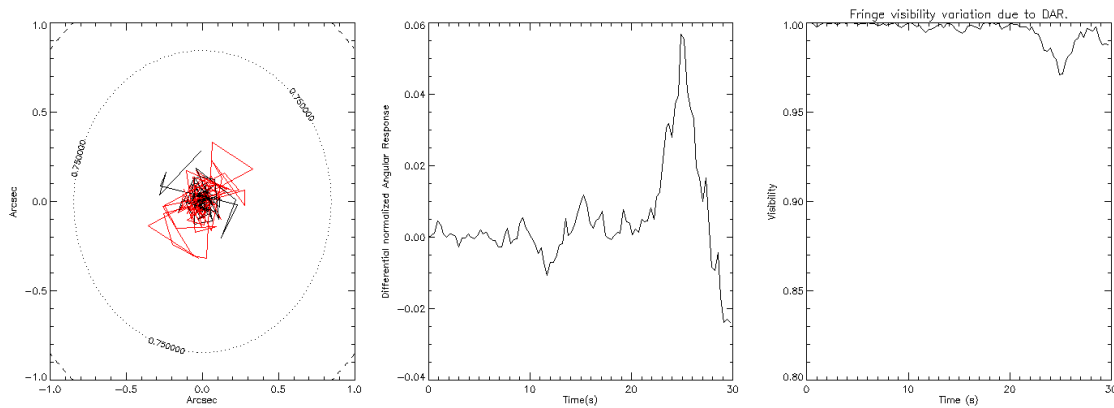
Figure 6. Simulation of the differential pointing (simulated naively as two independent Brownian motions). The range of variation can be seen to be contained within ~0.2" in a 30s span. In the centre, the differential angular response (normalized) for the source simulated (different – not independent curves apply for different positions). On the right how this affects the fringe visibility within an FTS scan. Additional pointing requirements could be attached for this effect.

2.5.3 Vibration and motion-induced phase errors

Physical causes being completely different from the above, the ultimate result will not be dissimilar to the phase difference described in (2.5.2) which can be categorized in a similar fashion (i.e. with offset plus relative phase difference map).

2.6 POINTING ERROR FREQUENCY AND TIME DOMAIN EFFECTS

2.6.1 Spectroscopic visibility and scanning speed stability

While this is not an attempt at an exhaustive explanation of phase correction and other issues related to drive speed non-linearities which occur in Fourier Transform Spectrometers, pointing errors will contribute to adding uncertainty to the spectral modulation.

Due to the separation in the frequency space of the spectral and spatial modulations, one can make use of the time quantities defined earlier to categorize (this time in frequency) the effects of pointing errors and other satellite related issues on the fringe visibility.

2.6.1.1 Effects occurring in T < τ

Vibrations occurring at timescales shorter than the detector time constant τ would have the effect of smearing out fringes in an un-recoverable manner. It is unlikely, however, that such fast vibrations (>100Hz) will be present in such large structures. Still, careful attention must be given to mirror mounts and active components such as the BSM to avoid generation and propagation of such frequencies.

2.6.1.2 Effects occurring in τ < T < Δt

Effects (if there are any) which occur in a time larger than the detector integration time constant, but shorter than the spectral scan time Δt, typically a few tens of seconds, are particularly disturbing and can potentially drive requirements on pointing variability in time. Such effects will impact on the time variation of fringe visibility within the single

spectral scan producing effects of amplitude modulation as well as adding uncertainty on the OPD variation with time.

Post processing can take into account errors in this range if they are well known. Metrological systems must therefore be devised to measure and record data concerning pointing and OPD variations. This will include highly precise pointing sensors, laser metrology systems, accelerometers, etc.

2.6.1.3 Effects occurring in $T > \Delta t$

Potentially the majority of the effects related to pointing errors or drifts, these errors do not affect the spectral content within the single uv-point observation but will vary the fringe visibility and phase reference between uv-points, hence impacting the spatial FT and image reconstruction. Applying the Marechal criterion, image reconstruction will require phase reference stability between u-v points of typically 0.05λ RMS, corresponding to $6\mu m$ OPD at $\lambda=30\mu m$. Translated into pointing accuracy, this corresponds to arcsin(dOPD/B) = arcsin($6\mu m$/100m) = 12mas.

3 TECHNOLOGY TRADE OFF

The satellite position requirements for the interferometer constituted by the hub and two telescopes relate to:

a) *Distance between the satellites.* In order to obtain the zero optical path difference using the ODL (Optical Delay Line), the positions of the two telescopes and the Hub must be into the range of the ODL, typically within 10 cm.

b) Oscillation around the relative position of the satellites. The optical path difference of the two beams must be known and stable to within a fraction of the wavelength, typically $\lambda/4$. For a minimum wavelength of $25\mu m$, the OPD must be controlled to within $5\mu m$. Requirements on its knowledge are higher based on the variation of the signal associated with such variation and is hence dependent on the derivative of the signal increasing the requirement on the tolerance.

c) *Attitude.* Attitude of the individual satellite must be controlled to a fraction of arcmin in order to allow the overlapping of the majority of the field of view of the single pixel from the two telescopes.

In the following we present briefly the state of the art of each of the three interferometer navigation models considered, formation flying, tethered, and structurally connected, allowing us to settle a choice of concept to be further detailed in the following chapter.

3.1 FORMATION FLYING

While a prevalent idea considers formation flight to be too expensive and far too complicated, it is still surrounded by a certain excitement, as was clearly demonstrated during the recent Conference on Spacecraft Formation Flying Missions and Technologies (5th SFFMT) organized by DLR in Munich, May 2013. So far, none of the proposed free-flyer projects of the precision class required for far infrared interferometry (TPF, Darwin, Pegase, FIRI, …) have been selected by their respective agencies. It is clear, as pointed out by Rupp et al (2013), that the system architectures poses great challenges in the areas of on-board sensing and actuation, high-level mission management and planning, as well as distributed fault detection, isolation and recovery, extending well beyond the theoretical precision and fuel expenditure calculations often put forward in the project presentations. Previous mission failures and terminations decrease the level of confidence in multi-satellite systems. Examples include NASA's Demonstration of Autonomous Rendez-vous Technology (DART) mission in 2005, which ended in an unintentional collision with the target satellite, and the U.S. Air Force TechSat-21 formation flying experiment in 2005, which was terminated due to technical issues "far more challenging than originally thought" (Rupp et al 2013).

The early free-flying experience indicates clearly the necessity of precursor technology demonstration missions for autonomous rendez-vous, proximity operations and formation flying. The PRISMA mission launched in June 2010 realized an important step towards practical implementation, when a large variety of flight tasks and guidance algorithms were demonstrated. In particular, aspects of formation flights relative to a non-interferometric

astronomy mission, NEAT, where a long-focal-length telescope objective is placed on a separate satellite from the detector satellite, were tested (Delpech et al 2013). With a separation of 12m and an accuracy target of 10cm, the requirements of such a mission are quite far from the performance required for an interferometric observatory. Still, reporting stability better than 4 cm (rms) during successive re-pointings between a set of celestial targets, the results obtained by this demonstration are promising, especially taking into account the stringent environmental and operational constraints of low orbit. Going to higher orbits and using finer equipment for both metrology and actuation should allow for considerable performance improvements (Delpech et al 2013). Still, it is clear that reaching navigation precision in the μm to mm range, for which the use of optical rather than radio-frequency navigation sensors will be necessary (Rupp et al 2013), will require considerable development efforts

3.1.1 Conclusion

Formation flight appears immature at this point an will require large development efforts to become practical at the level of precision required. We therefore do not consider this technology for the present study. Developments in this field should be closely followed, however, and it will certainly represent a promising, and even obligatory, technology for the distant prospects of kilometric and supra-kilometric interferometers.

Figure 7. The TANGO satellite of PRISMA seen by the MANGO satellite. Credits: OHB Sweden

3.2 TETHERED FORMATION

The early idea dealing with the use of tethers in the spacecraft formations flying are from the 1970s and 1980s (Bainum, 1972; DeCou, 1989). The studies are focused on the concept

of the tethered configuration concepts without considering the tether dynamics and control. Detailed analyses on the dynamics of tethers for formations spinning about their bore sight, on the retargeting of the spinning formation attitude and on the stabilization of the individual tethered units of the formation were conducted successively (Bombardelli et al., 2004a; Kumar, 2004). Analysis that makes use of the knowledge acquired from a number of tether missions in Low Earth Orbit (LEO) (Lorenzini, 1987 and 1990) led to the development of the SPECS study (Lorenzini et al. 2006).

Dynamic analysis and control of tethered formations has been reported, indicating that further development and testing of tethers in space will be necessary as a first step toward the implementation of a Far Infrared Interferometer due to its severe requirements on angular resolution and image quality.

In principle, the interferometer rotation to cover all the u-v plane can be achieved at constant angular momentum about the beam combiner with no propellant consumption. In practice, thruster fuel is used to keep the tangential velocities constant and to reposition the orbital plane to acquire new astronomical targets and to correct the attitudes of the spacecraft and beam combiner.

To avoid noise in the spectroscopic measurements, the satellite oscillations around the ideal relative positions should not have frequencies higher than the fringe tracker bandwidth, which depending on the specific design and conditions. This noise perturbs the spectroscopic measurements by means of a jitter effect; in particular the noise to consider is in the band $(3 \cdot 10^{-2} - 10 \text{ Hz})$ where the spectroscopic measurements are performed.

Compared to a free-flyer system the tethered one con rotate at a higher rate, showing better stability (gyroscope effects) so as to be less sensitive to external perturbation and improve the system pointing.

In principle an interferometer with tether connection from the point of view of its dynamic can be considered as a system with boom connection especially for what concern its operation. It can be operated maintaining a constant angular momentum during the coverage of the u-v plane, without consuming propellant, or at tangential velocity constant, managing the tangential thrusters, so to permit to the collectors to operate within the desirable range for image synthesis.

The retargeting of an interferometer with tether connection can be obtained using thrusters disposed in the telescope and able to give harmonically varying forces.

As an example: for a collector mass of $3200 kg$ at a distance of $500 m$ with tangential velocity equal to 2.15 m/s, an angle $\vartheta_\mathrm{p} = 3°$ is obtained in three complete rotations of the system in $1 hour$, with the two thrusters, acting out-of plane and in plane, with a maximum value equal to 0.164 N.

Propellant total mass to cover the whole 95.5 radians of retarget angle in the course of a mission, at a tangential speed of 2.15 m/s amounts to less than 1%, or about 27 kg of fuel per collector equal to about the 6% over the mission lifetime.

Specific requirements concerning the use of the tethers are connected to its survival in the space environmental in L2 during the mission duration of 5 Years. In order to increase the probability to survive to micrometeoroids in L2, the tether has been designed not as a single line (single failure) but in a multi-line shape. In particular has been studied different combination of line: one line tether; 2-parallel line interconnected every 100 m; 4-parallel-line interconnections within each tether branch.

3.2.1   Conclusions

Preliminary analysis demonstrated the possibility to use the tether for the implementation of a FIR Interferometer as the one conceived for SPECS, but further analysis and experimental activity are necessary regarding the followings topics:

- Damping of tether vibrations;
- Reconfiguration of the baseline;
- Retargeting;
- Positioning of the spacecrafts to better than 10 cm during observations;
- Measurement of accelerations transmitted by tethers to the satellites;
- Minimization or cancellation of torques transmitted by the tether to the spacecraft, through center of mass or attachment point control.
- Tether technology development in ground experiments and flight demonstration at short and long tether lengths.

3.3   STRUCTURALLY CONNECTED TELESCOPES

The most conservative approach to long-baseline interferometry in space is the structurally connected design. Here, deployable booms constitute a rail on which the two telescopes are wheeled in and out in order to cover a range of baseline dimensions. Light-weight booms will most likely be made in the form of a truss structure, benefiting from high stiffness and low weight. These can be devided into segments and packed into the fairing of a launch vehicle, as in the ESA-CDF study (ESA report 2006) and in the SPIRIT proposal (Leisawitz et al 2010), see Figure 8. The maximum baseline for this concept is 36m. The same approach on a smaller scale (8m baseline) is currently being built as a bolloon-borne experiment (Reinhart et al 2014), see Figure 9.
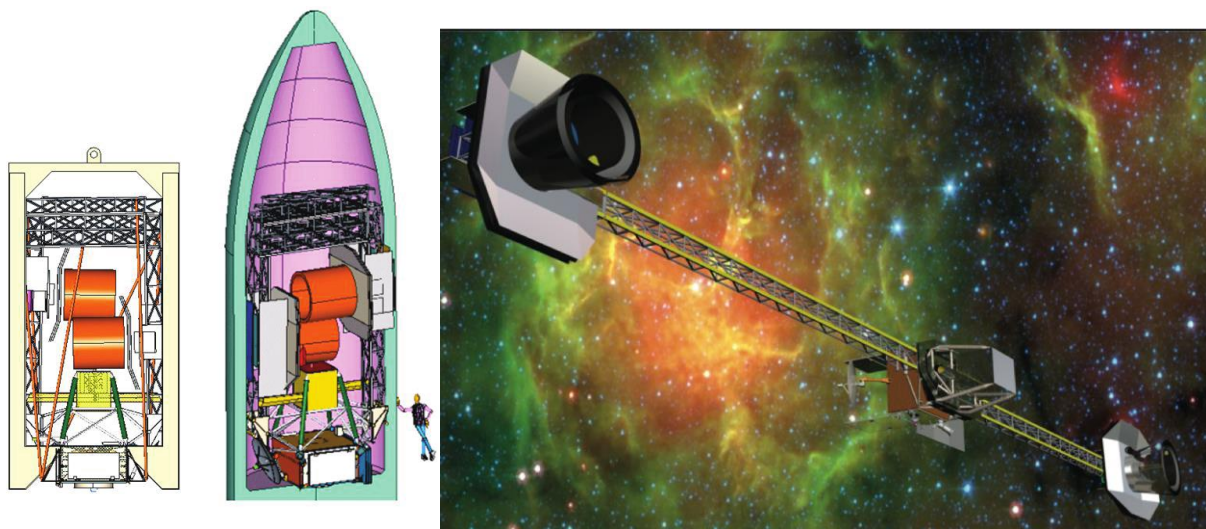
Figure 8. Stowed (left) and deployed (right) truss structure for the SPIRIT proposal (Leisawitz et al 2010).
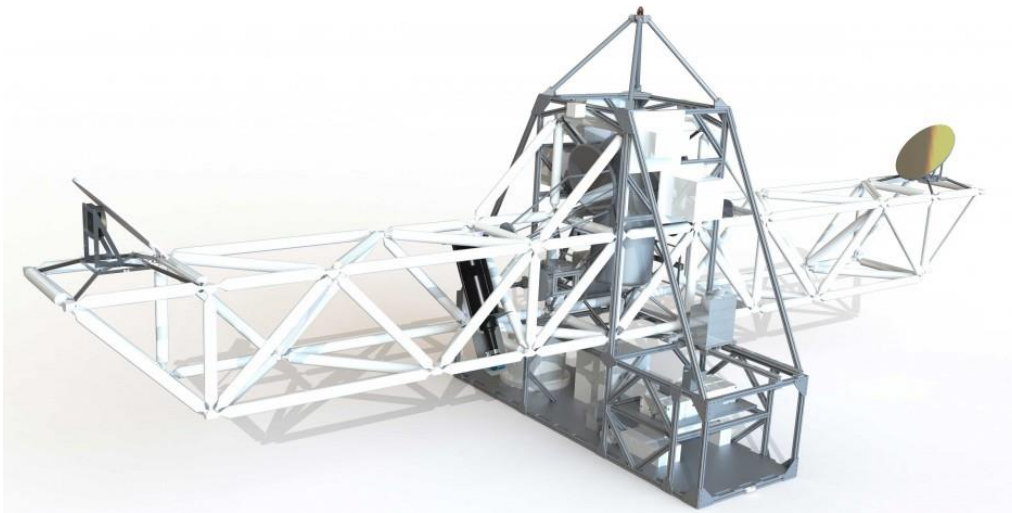
Figure 9. The BETTII balloon-borne interferometer (Reinhart et al 2014).

Truss-based constructions in space have been much developed, notably in the case of the international space station built around a truss of total length 109m [NASA ISS website], see Figure 10. Ongoing developments of deployable truss structures with extremely compact launch configurations, such as the ADAM collapsible truss system from Able Engineering Inc. (Tibert 2002), provides hope for extension of the SPIRIT concept towards the 100m baseline considered in the FISICA study. The ADAM system is deployed as shown in Figure 11 resulting in a space-proven and highly scalable structure, the longest example of which reached nearly 61 m. Another example, shown in Figure 12, is ROCCOR collapsible and roll-able truss using composite slit-tube booms as a repeating structural unit. This patent pending design offers high packaging efficiencies and outstanding deployed properties (bending and torsional stiffness and strength). The joints between longerons, battens and diagonals do not need to articulate allowing simplified connection methods (riveting, ultrasonic welding, bonding) leading to high manufacturing efficiency and reduced cost.

Figure 10. The international space station, built around a 109m long truss.
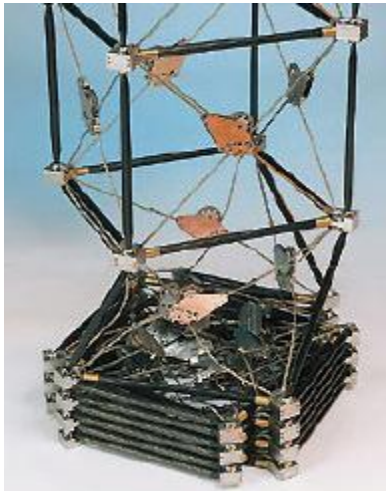
Figure 11. The ADAM collapsible truss system from Able Engineering Inc. (Tibert 2002).
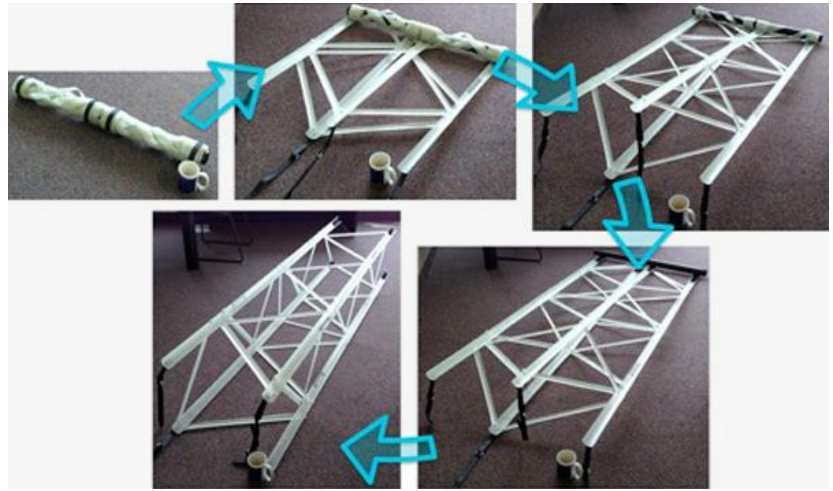
Figure 12. The ROCCOR collapsible and roll-able truss [ROCCOR web site].

3.4   TRADE-OFF SUMMARY AND CONCLUSION

Following this review of current status for formation flight, tethers, and trusses, we conclude that for the current proposal of a 100m baseline structure, the most technologically advanced option is the stiff truss structure. Such structures are routinely used up to these dimensions and on-going developments promise hope for extremely compact launch configurations.

For longer baselines, possibly up to 1km, tethers are expected to provide an excellent alternative. Formation flight, still considered immature for the precisions required for interferometry, will probably be mandatory for supra-kilometric larger baselines.

4 DETAILED STUDY OF THE CONNECTED STRUCTURE OPTION

4.1 INTRODUCTION

In this section the study connected to the interferometer in the conditions of the two satellite mechanically interconnected will be analysed in detail, particularly the case of a rigid truss to the identification of the algorithms necessary to maintain satellite positions and comparison with positional requirements, and requirements on the AOCS. The team from AGI with experience of similar on board systems conducted this effort using inputs from INAF-IAPS and substantial coordination with LAM, where development of a metrology test-bed has taken place.

It is necessary to remark that the similarity between the satellites interconnection with tethers and mechanical boom is very strong and several considerations here reported for the boom interconnection can be retained also for the tethers configuration.

4.2 METROLOGICAL PROBLEMS OF THE INTERFEROMETER AND ITS DYNAMICAL CONTROL.

The gravity gradient acting on the interferometer placed in the Lagrange point L2 (candidate orbital location) is very small and so the relevant accelerations present on the interferometer are those due to its rotation performed around the ILS (Instrument Line of Sight) combined with the variation of the ITD. In this condition accelerometers installed on the telescopes can measure directly their tangential and centrifugal acceleration, related to the ITD and to the rotation angles (determined by the star sensors); by means of a feed-back system, this information can be used to control the thrusters, so to force the system to follow an opportune control law, for the variation of the ITD and angular velocity. The control can give the possibility of the acquisitions of the u, v points in the minimum time and best conditions optimized for the relative observation mode.

Together with the analysis of the control laws for the telescopes of the interferometer, it is necessary to take under control the metrological problems for the accuracies required in the measurement and/or determination of the relative distance between the telescopes and the requirements for the levels of noise present on them, so to keep the noise for the Optical Path Difference (piston, tilt and wave-front error) within the levels required for the visibility of the interferometer. Placed in the Lagrange point L2, the interferometer is maintained in this position by means of traditional techniques of attitude control, to which will also be entrusted the task to point the telescope towards the observed sources. In the next phase of operation of the interferometer, it will rotate around the axis passing through the sources and for its HUB (axis ILS$_{HUB}$), reducing the distance between the two outer satellites-telescopes ($R_1(t)$, $R_2(t)$) so to cover the u-v plane.

In a first idea the two satellites go through a spiral at a constant tangential velocity (about one meter in $25s$) with an appropriate control law that will govern the distance between the two telescopes and the rotation speed of the interferometer, so to ensure maximum coverage of the $u - v$ plane, in respect of its functionality from both the spatial and spectroscopic point of view; it is clear that also other modalities to cover the u-v plane will be considered, as for example to readjusting the satellites baseline every half turn. In L2 the dominant accelerations acting on the interferometer are essentially the inertial

accelerations, determined by its rotation, in particular the centrifugal accelerations are of the order of 10^{-3}g. The measurement of these accelerations with precision of 10^{-8}g, should allow the control of the system (this at least for the tethered and booms connection between the two telescopes) through the variation of the distance between the two satellites and its rotation, in accord to the law of conservation of its momentum. The variations of these accelerations are expected at periods of about 24 hours, which represent the estimated time to walk the spiral so to cover the entire plane $u - v$. Also, we can underline the fact that the difference between the two measured accelerations is connected to the angular system rotation and to the distance between the two points at which the radial accelerations are measured:

$$a_d = \omega(t)^2 \cdot R(t),$$

Where

$$R(t) = R_1(t) + R_2(t)$$

The formula gives the opportunity to recover the absolute distance between the two telescopes, if ω is measured (star sensors or gyroscope).

In Figure 13 is reported a general scheme of the possible control loop for the dynamic control of the interferometer; the system is monitored by means of an IMU that gives information on the interferometer angle rotations, and to the accelerometers that monitor the centrifugal and tangential accelerations. The monitored values will be compared by the ones coming to a control law and the error values are sent to the actuators (thrusters and step motor).
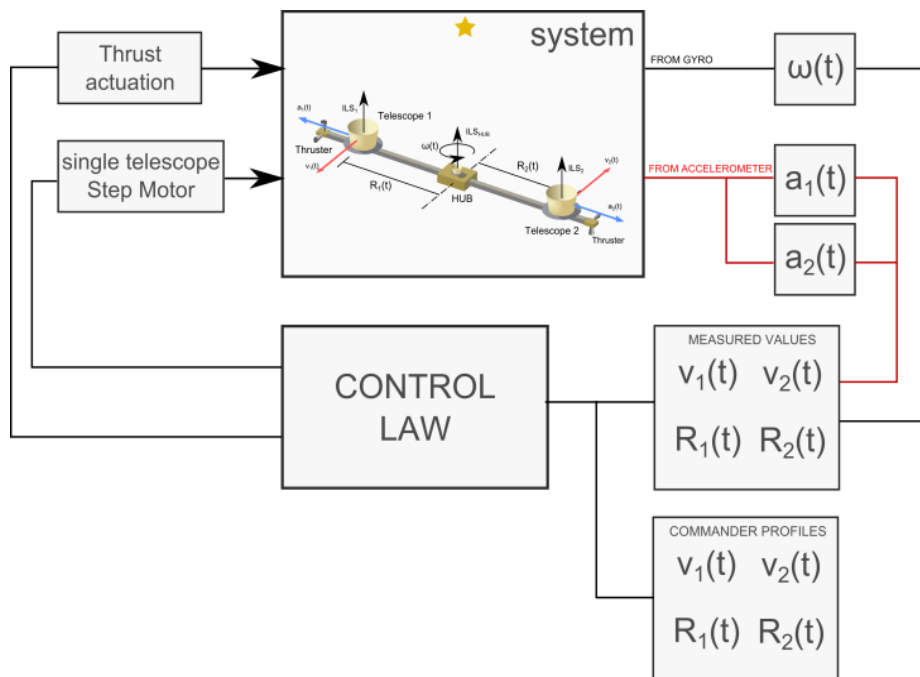
Figure 13. Possible scheme of the interferometer control loop

4.3 Acceleration in L2

In this subsection we report the first analysis concerning the evaluation of accelerations acting on a system of satellites disposed in L2, due to the gravity gradient and to the system dynamics necessary to cover the uv plane, in particular are evaluated the acceleration acting on a system of two telescope satellite connected to a central hub by means of a mechanical interconnection (boom supports). It is necessary to remember that the analysis holds also for the tethers connection.

This analysis is of fundamental importance because it excludes the effects of the gravity gradient on the system, leaving the necessity to control the interferometer, during the science observation only for what concern its dynamic. This activity, as well as the majority of the activity reported in the following subsections are connected the task_2.2 "Satellite positioning tolerance based on accelerometer control loop", which main objective is the examination of the technical challenges in implementing closed loop accelerometer feedback for satellite position control so to satisfy positional accuracy requirements and principally to implement a control law so that the satellite system positioned in L2 will move so as to satisfy the requirements in order to perform the scientific observations, i.e. the right movements to cover all the uv plane.

4.3.1 Gravity gradient accelerations acting on the FIR Interferometer in L2 Orbit

Using the Eulero-Hill formulas it is possible to evaluate the differential gravity acceleration acting between two satellites orbiting in L2; acceleration that must be imparted by the orbital control on the satellites so to maintain their distance fixed.

A reference having its origin in the center of rotation of two satellites, arranged as shown in Figure 14, with the x axis oriented as the Earth-Orbit joining, the z axis normal to the ecliptic and y to complete the right-handed triad, it is in rotation with respect to an inertial reference frame, because it rotates at about to the speed with which the trajectory of the point L2 completes a revolution around the Earth.
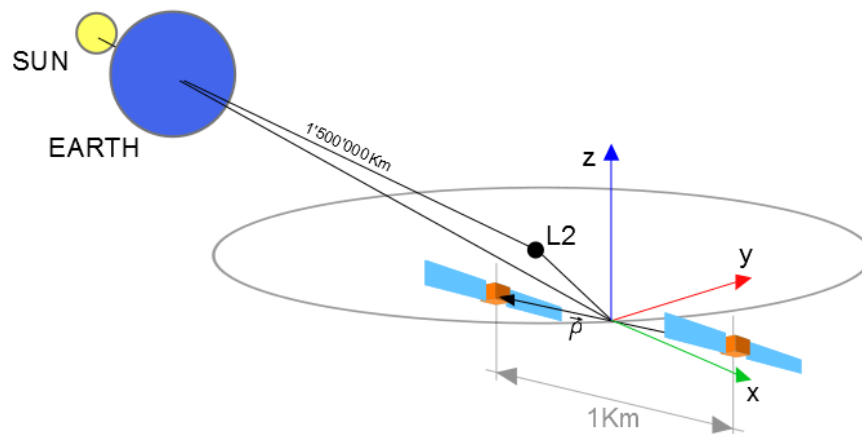
Figure 14. Eulero reference frame.

In the described reference, you can write the equations of motion of a satellite as composed by the difference between the attraction took place to the center of the reference and the

one acting on the satellite itself and being a non-inertial reference frame, it must consider also the apparent acceleration:

$$\ddot{\vec{\rho}} + 2\vec{\omega}_0 \times \dot{\vec{\rho}} + \dot{\vec{\omega}} \times \vec{\rho} + \vec{\omega}_0 \times (\vec{\omega}_0 \times \vec{\rho}) = \underline{\underline{G}} \cdot \vec{\rho}, \qquad\qquad 1)$$

where ρ (t) is the position vector of the satellite in the given reference, ω (t) is the speed of rotation of the reference with respect to the fixed stars, and G is the tensor of gravity, which has its origin in the center of the reference.

Near the L2 point, the gradient of gravity can be considered as the sum of the action of the Sun and Earth and because they are aligned, their effect is superimposed perfectly and can be easily estimated:

G = G$_E$ + G$_S$ = μ$_E$D/R$_{Es}$³ + μ$_S$D/R$_{Ss}$³,

where D is the initial distance of the satellite in the initial reference and R_{Ss} and R_{Es}, respectively, the distances Sun-satellite and Earth-satellite. If the distance D (approximately ρ) is of the order of 1 km (as in the free-flyer system), then, for L2 G_E will be of the order of $2 \cdot 10^{-10}\ m/s^2$ and $G_S = 3 \cdot 10^{-11} m/s$.

The equation_1, can be integrated and the positions $x\ (t),\ y\ (t),\ z\ (t)$ of the satellite will be found as solutions of the following three equations:

$$\ddot{x} - 2\omega\dot{y} - 3\omega^2 x = 0$$
$$\ddot{y} + 2\omega\dot{x} = 0 \qquad\qquad 2)$$
$$\ddot{z} + \omega^2 z = 0$$

Parameterizing and normalizing, it is found:

$$x = A\sin\tau + B\cos\tau + 2K$$
$$y = -3K\tau + 2A\cos\tau - 2B\sin\tau \qquad\qquad 3)$$
$$z = C\cos\tau + D\sin\tau$$

Where the A, B, K, C and D are coefficients depending on the initial conditions, given by:

K=v$_{y0}$ + 2*x$_0$;
A=v$_{x0}$;
B=-2*v$_{y0}$-3*x$_0$;
C=z$_0$;
D=v$_{z0}$;

It is seen that the movement in the direction out-of-plane, z, is totally decoupled from the rest of the motion. As regards the movement in the plane, to have a stable motion, that is, a trajectory perfectly closed, the coefficient K must be equal to 0, that is worth the constraint between the initial conditions: $V_{y0} = -2x_0$. Thus, even for an unperturbed motion, where the reference center is in L2 and it has a perfectly circular orbit around the earth, the satellite would tend to make an elliptical path, as shown in Figure 15. This is due to the

form of the acceleration in the second member in 1), where the gradient of gravity G has a form of an ellipsoid of rotation. In the **Figure 16** is shown the relative distance between two satellites without interconnection, orbiting L2.
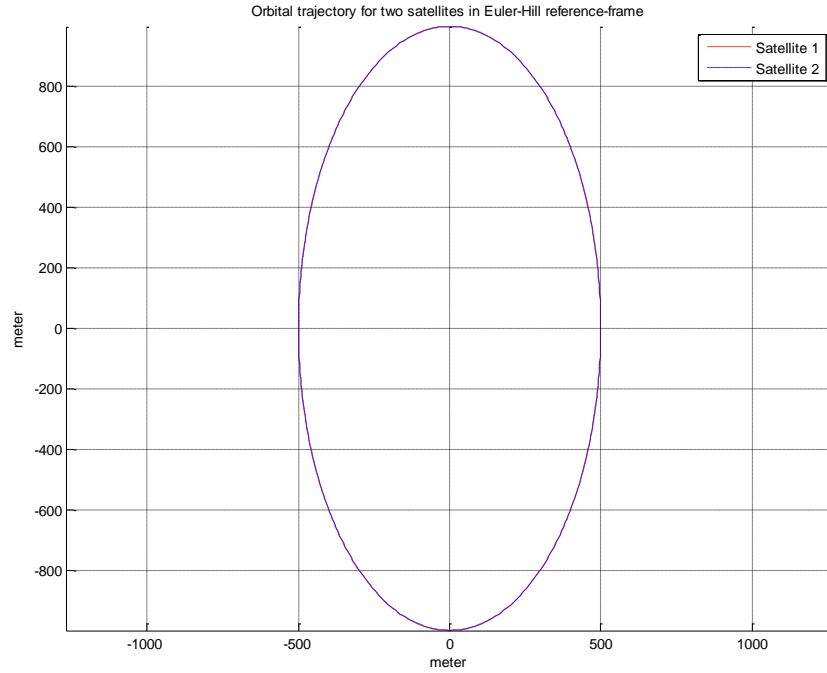
*Figure 15. **Elliptical trajectory of two satellites out of phase by 180 ° in a Euler non-inertial reference frame.***
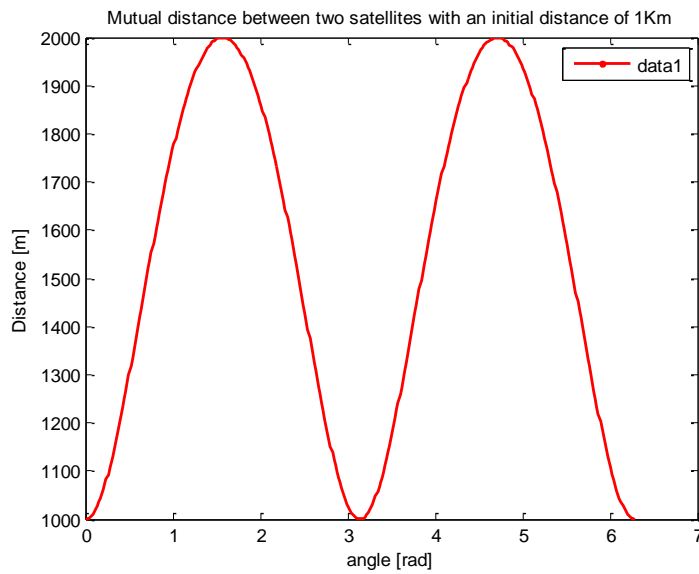
*Figure 16. **Relative distance between the two satellites not interconnected orbiting in L2.***

So, for two satellites disposed on the plane with a phase-shift between them of 180 $degrees$, in free fall, the distance between them change in time, harmonically oscillating between 1000 and 2000 m. To keep the satellite at the same distance, their orbit must therefore be controlled through an acceleration that is always of the same order of magnitude as the natural force, ie about $10^{-10} \ m/s^2$ and at the orbital period, as it is shown in the Figure 17.
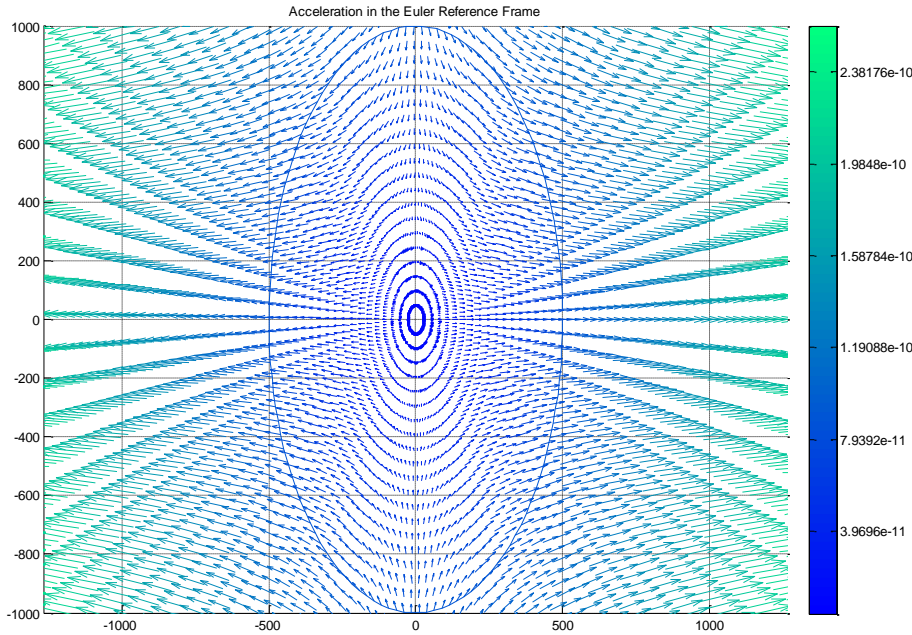
Figure 17. Accelerations in the Euler reference frame in L2, due to the gravity gradient.

The frequencies, at which these accelerations must be implemented, will depend on the control system and to the shape of orbit that one wants to control and to the manoeuvres that one wants to implement; due to its complexity the problem cannot be here solved.

4.3.2   Interferometer dynamic in L2 – Spiral trajectory

It is clear that if you like to force a system of two satellites in L2 to follow a particular trajectory, in first approximation you can forget about the acceleration necessary to compensate for the gravity gradient change and take into account only the accelerations necessary to give the desired dynamics to the satellites. In the following we like to give a simple evaluation of the acceleration necessary to apply on a system of two satellites placed in L2, to force them to describe a spiral, so to cover the complete uv plane. In the following formulas the spiral equation in a plane x, y where the motion is performed are reported:

$$x(t) = D\left(1 - \frac{t}{T}\right)\cos(\omega_T t) + \frac{D}{T\omega_T}\sin(\omega_T t)$$
$$y(t) = D\left(1 - \frac{t}{T}\right)\sin(\omega_T t) \qquad\qquad 4)$$

Where T is the period of reference with which the trajectory is travelled, $\omega_T = \frac{2\pi}{T}$ is the angular velocity, while D is the initial distance of each satellite from the centre of the reference.

If the characteristic time in which to accomplish the trajectory is of the order of 24 hours, in the equation (4), then, with respect to the angular velocity of the reference Euler $\omega \ll \omega_T$. Whereby, the accelerations to impart to the satellite by the control system will be decoupled from the one necessary to control its dynamics. Trajectory, speed and acceleration in the x, y plane are described in Figure 18.

During the maneuver, the maximum acceleration that the control system must impart so that the satellite remains on the spiral, is of several orders of magnitude larger than those required to stabilize it in L2. From the figure_5.2.2-1 we see how they vary in time, assuming the maximum value equal to approximately $3 \cdot 10^{-6} \ m/s^2$.
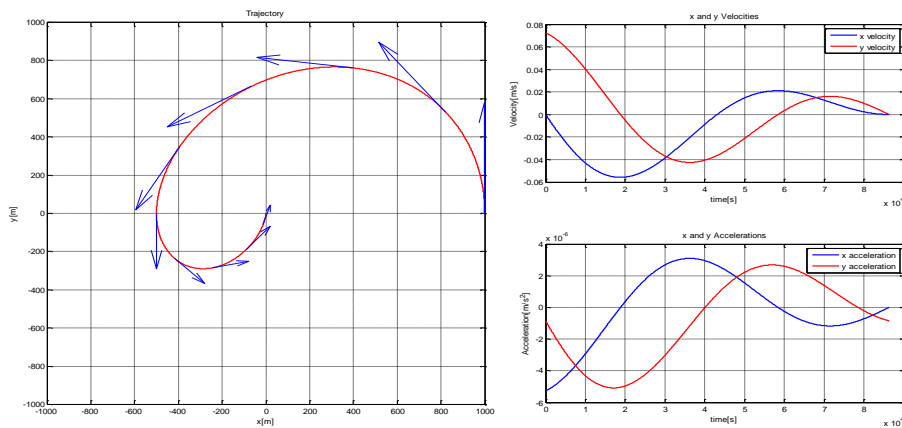
Figure 18. *Trangectory speed and acceleration for the spiral to be followed by the satellite*

For completeness we list the formulae for speed and acceleration in the x, y plane of the trajectory:

$$\dot{x}(t) = -D\omega_T \left(1 - \frac{t}{T}\right)\sin(\omega_T t)$$
$$\dot{y}(t) = D\left(1 - \frac{t}{T}\right)\cos(\omega_T t) - \left(\frac{D}{T}\right)\sin(\omega_T t)$$

$$\ddot{x}(t) = -D\omega_T \left(1 - \frac{t}{T}\right)\sin(\omega_T t)$$
$$\ddot{y}(t) = D\left(1 - \frac{t}{T}\right)cos(\omega_T t) - \left(\frac{D}{T}\right)sin(\omega_T t)$$

The main results is that the acceleration is of the order of $8 \cdot 10^{-4} \ m/s^2$, several order of magnitude bigger than the one acting on them due to the gravitation in L2.

4.4 INTERFEROMETER OPERATION MODES

To balance centrifugal spinning forces, we consider a FIR Interferometer telescope constituted by two telescopes and a central hub connected with booms (analogue analysis is valid also for tethers), see Figure 19. In the Figure 20 the same telescope with the

indication of the observation plane, perpendicular to the ILS (Instrument Line of Sight) is shown, on which the dynamic of the interferometer is performed. The interferometer rotates around the ILS vector at the hub.
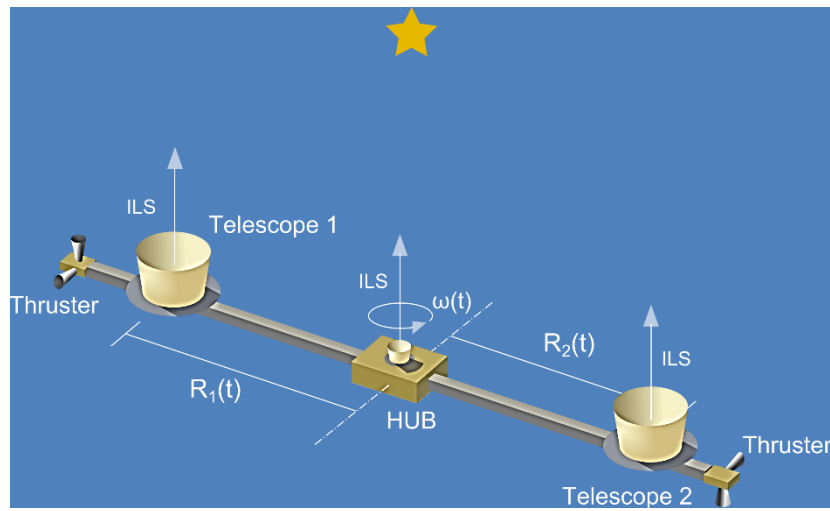
Figure 19. FIR Interferometer telescope constituted by two telescope and a central hub connected with two booms.
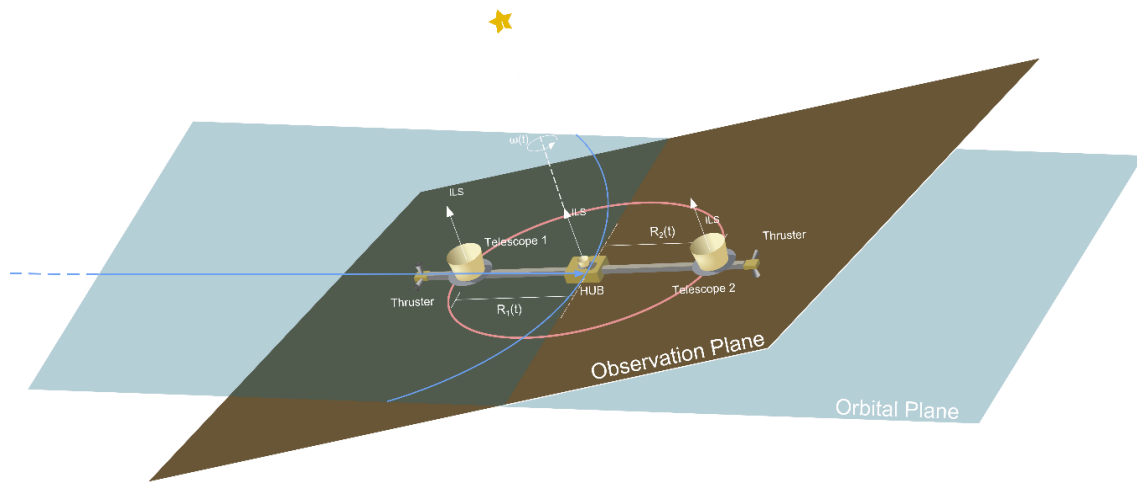
Figure 20. Boom connected FIR Interferometer telescope with indication of the observation and orbit planes.

Here we analyzed the dynamics of the system: spinning velocity, centrifugal forces, axial tensions, in order to find the optimum in terms of required time, propellant consumption, and optimal coverage of the u, v plane. We analyze the system as constituted by two equal ideal mass representing the telescope, which can move in the observation plane linked together by the booms. The central Hub has an internal motor permitting to change the ITD $R_1(t) \ and \ R_2(t)$.

As the system will be a sort of big gyroscope it will conserve his angular momentum, while the angular velocity and the tangential velocity will increase and decrease with a fixed law, a function of the boom length and time. Here we studied the temporal law by which we can

change the ITD, in order to respect the constraints imposed on the acquisition of all the uv points. The analysis of the problem will start by finding the law that links the ITD of the two telescope to the angular velocity and tangential velocity.

Given an initial angular velocity of the system, the angular momentum can be write:

$$b = I_S\omega \qquad\qquad 1)$$

Where I_s is the Moment of Inertia of the system and ω is its angular velocity.
Without loss of information, here the system is considered as ideal, and we write its moment of inertia as for concentrate masses:

$$I_S = 2MR^2 \qquad\qquad 2)$$

Referring to Figure 19, the R in equation (2) is the average of the two distance R_1 and R_2: $(R_1 + R_2)/2$. In a more complex behavior, I_S and the center of rotation have to be accurately measured.
For the ideal case we can use the equation 1), as a base to consider how the system evolves, if a motor inside the Hub start to change the R_1 and R_2 distances. We can suppose for the moment, that the same law is applied contemporary to the two telescopes, so the problem can be reduced to the study of only ones of the two bodies.
The equation 1) became: $b = 2M\omega R^2$

This quantity must be conserved vs time when the radius $R(t)$ will be changed: $\frac{db}{dt} = 0$.

$$\frac{db}{dt} = 2M\frac{\partial\omega}{\partial t}R^2 + 4M\frac{\partial R}{\partial t}R\omega = 0$$

 it follows:

$$\frac{\dot{\omega}}{\omega} = -2\frac{\dot{R}}{R} \Rightarrow \ln(\omega) = -2\ln(R)$$

$$\omega(t) = \frac{C}{R(t)^2} \qquad\qquad 3)$$

Evaluating the equation 3) and considering that the tangential velocity of the telescopes trajectory is $v_t(t) = \omega \cdot R(t)$, it follow:

$$v_t(t) = \frac{C}{R(t)} \qquad\qquad 4)$$

From the last equation we can easily deduce that it is impossible to get a constant $v_t(t)$ if $R(t)$ changes *vs* time.
In the next sections we analyze the two following possibilities:
   a) Changing the distance R(t) and leaving the system to change its angular velocity consequently (so to avoid consume of propellant), but ensuring the cover of the uv plane with an appropriate tangential velocity.

b) Changing the distance R(t) with the introduction of a simultaneously momentum, so to maintain the system on a spiral and conserving the appropriate tangential velocity.

4.4.1 Changing the distance R(t) without thruster assistance

In this section the possibility to change the distance $R(t)$ between the two satellite and the hub will be considered, leaving the system to change as a consequence its angular velocity. In order to ensure the complete coverage of the uv plane with an appropriate tangential velocity, we will select an appropriate law for $R(t)$, considering a diameter for the telescopes mirror of about 2 m. In this case it is not necessary to use thrusters, so avoiding to consume propellant. To do that, we must consider how much time the measure takes, and the R_{max} and R_{min} of the plane to cover.

Let's start with a linear law for the ITD change:

$$R(t) = A + Btn \qquad\qquad 5)$$

The constant C relates to the initial velocity of the system. So, if we imagine to require a mean step of about the half of the telescope diameter D, we can say that we need about $N = 2*(Rmax - Rmin)/D$, rotations of the system.

Considering a scheme of the interferometer as shown in the Figure 21 we studied the cover of the u, v plane for a single telescopes that moves with angular velocity $\omega(t)$, with a distance from the center $R(t)$, starting at $Rmax$ at $t_0 = 0$ and stops at $Rmin$ after $T = 86400\ sec\ (1\ day)$. If is $D = 2\ m$, and $Rmax = 50\ m$ and $Rmin = 10\ m$, we can easily consider $N \approx 40$, that means that, at the final time T, θ value is θ(T) = N*2π.
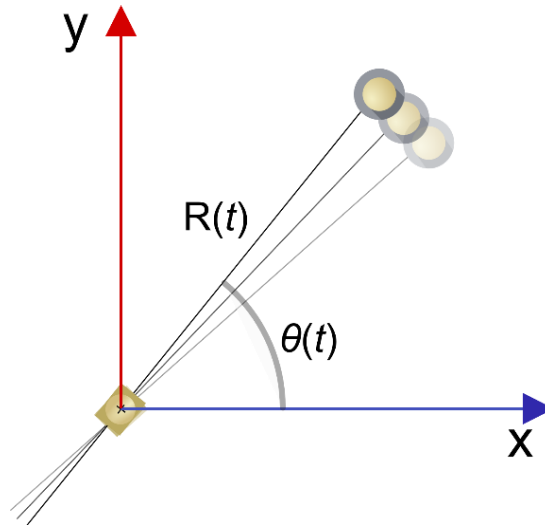
Figure 21. Schematic of the interferometer for its dynamic analysis

So, we can find the constants A, B and C, imposing the boundary conditions:

$t=0$	$t=T$
$R(0) = R_{max}$	$R(T) = R_{min}$

$\theta(0) = 0$	$\theta(\text{T}) = \text{N}*2\pi$

where the condition on $\theta(t)$ is imposed resolving the following integral, and introducing the constant E:

$$\theta(t) = \int \omega(t)dt = C\int \frac{1}{R(t)^2}dt + E \qquad\qquad 6)$$

The constant A and B can be found using the boundary conditions on radius:

$$A = \frac{R_{max}t_{fin}^n - R_{min}t_{in}^n}{t_{fin}^n - t_{in}^n}$$

$$B = \frac{R_{max} - R_{min}}{t_{fin}^n - t_{in}^n}$$

The integral in equation 2 can be easily resolved using a basic 1th degree Newton-Cotes rule, if R(t) is a low order polynomial:

$$\theta(t) = C\int_0^t \frac{1}{R(t)^2}dt + E = C\frac{1}{2}\sum_{t_i=0}^{t_i=t}\left(\frac{1}{R(t_i)^2} + \frac{1}{R(t_{i+1})^2}\right)(t_i - t_{i+1}) + E$$

$$(7)$$

$$\theta(\text{T}) = C\int_0^T \frac{1}{R(t)^2}dt + E = C\frac{1}{2}\sum_{t_i=0}^{t_i=T}\left(\frac{1}{R(t_i)^2} + \frac{1}{R(t_{i+1})^2}\right)(t_i - t_{i+1}) + E = 2N\pi$$

Once the constant C is found the initial conditions of the problems are imposed and the angular and tangential velocities profiles can be easily found using the equations 3 and 4.

4.4.2 Numerical Simulations for different ITD variations law, without the thrusters assist.

In this section we focused on a series of ITD changing laws R(t) leaving the interferometer to change its tangential velocity. Referring to the previous equation 5, we solve for a low order n: 1, 2, 3 and ½ and an for an exponential law, $R(t) = Ae^{Bt}$.

In the following figures are plotted for the five selected laws, respectively: the radial displacement, the velocity, the centrifugal acceleration, and the radial steps that the telescope does after every rotation of 360°.
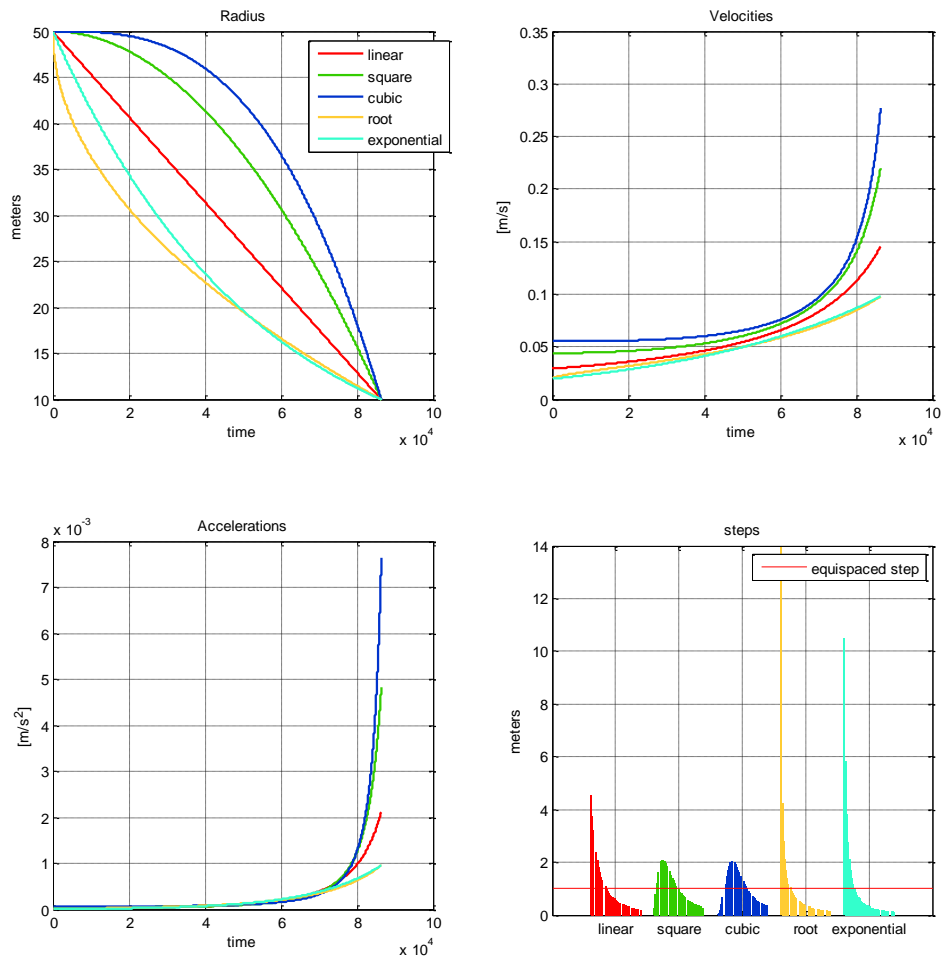
*Figure 22. **Plots for the five selected radial variation laws, respectively of the radial position, the velocity, the centrifugal acceleration, and the radial steps, that the telescope does every rotation. In red linear law, in green the square, in blue the cubic, in yellow the square-root and in cyan the exponential one.***

In the following figure is plotted for the five selected laws, the trajectory of the telescopes.
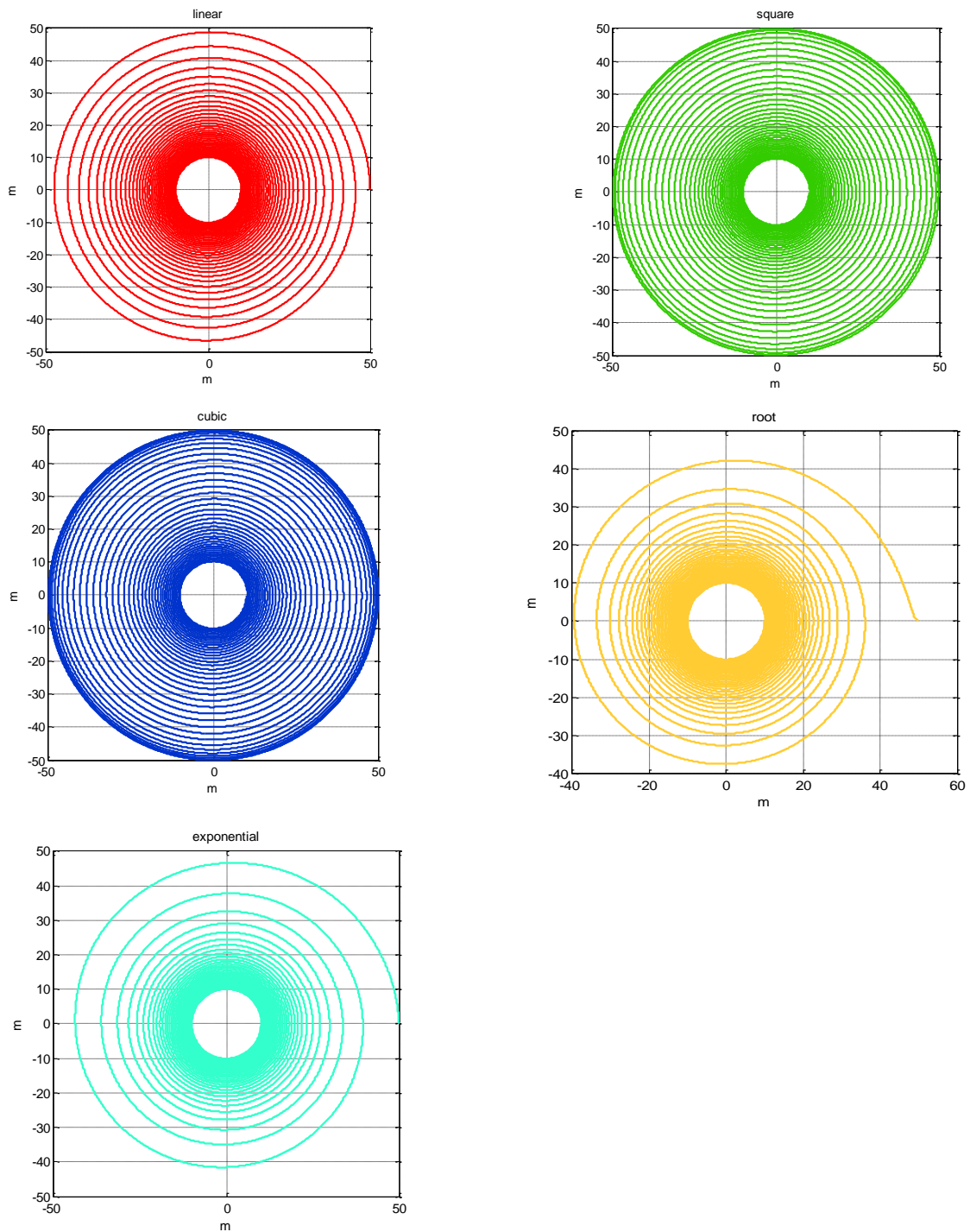
Figure 23. **The five trajectories. In red linear law, in green the square, in blue the cubic, in yellow the square-root and in cyan the exponential one.**

As we can see, the cubic law is the one that better fits the need to have the most regular step length during the rotation. But the square law also offers a good coverage. For the cubic and square laws, in the next figures, we report the results for the acceleration and the coverage on the rotation plane. If we compare the cubic and square cases, we can see that

the u-v coverage is quite similar, but the centrifugal acceleration, and consequently the tension during the rotation, is reasonably less for the square case than for the cubic.
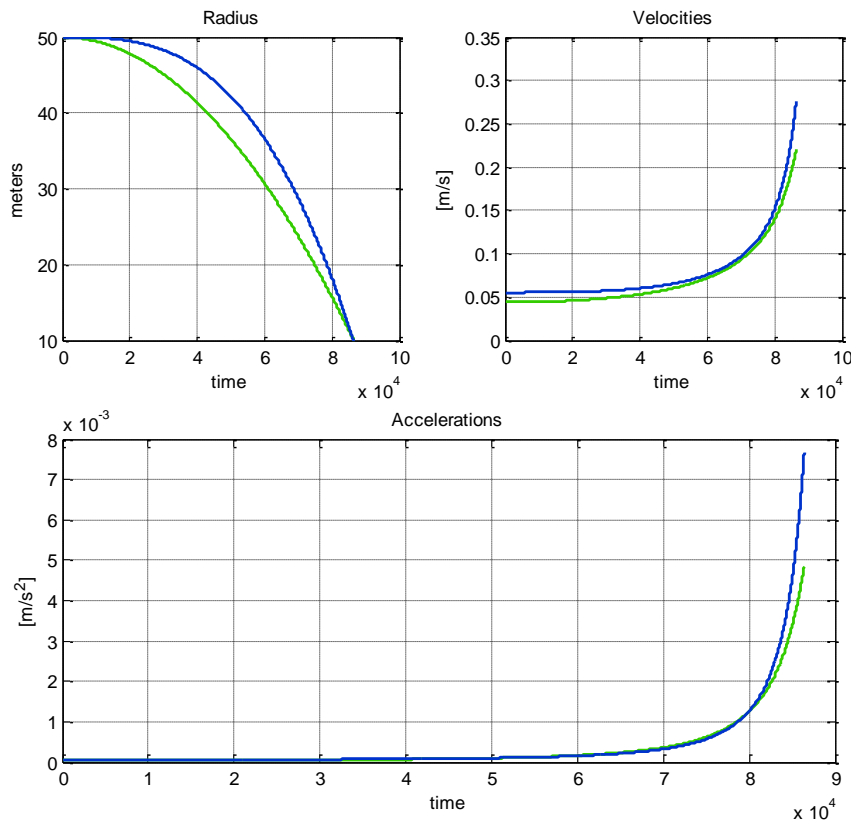
Figure 24. **Velocities and Centrifugal accelerations for the cubic and square law.**
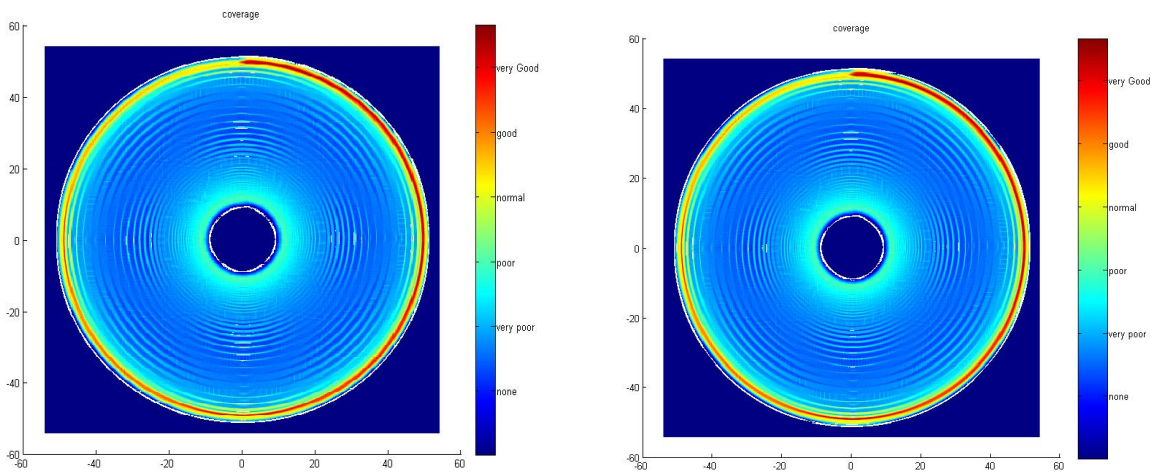
Figure 25. **Coverage of the u-v plane for the square law (left) and cubic law (right) considering a telescope dish of 2 meters.**

4.4.3 Changing the distance R(t) with thruster assistance

During this work it's just demonstrated that a change in radial distance of interferometer telescopes results in a change of associate angular and tangential velocity. So, in order to get the goal to reach a constant tangential velocity along a spiral trajectory, the system should change its angular momentum continuously during the manoeuvre. In this condition we calculate the requested momentum to be applied to the whole system in order to maintain the same tangential velocity of the telescopes, during the entire trajectory.

Our constrains are a constant v_t and a constant distance P between the different turns described by the telescopes. In formula:

$$v_t = cost$$

$$N = \frac{(R_{fin} - R_{in})}{2\pi P} \qquad\qquad 8)$$

where N is the numbers of rotations. In this work we assume that a $P = D/2$, the half of the telescope's dish, is good enough for the overlapping of the two telescope field of view necessary for the interferometric purpose.

Under those conditions the radius R has a linear dependence with the angle θ, and can be written:

$$R(\theta(t)) = R_{in} - \frac{(R_{fin} - R_{in})}{2\pi N}\theta(t).$$

Substituting in it the value obtained from equation 8) we get:

$$R(\theta(t)) = R_{in} - \frac{D}{4\pi}\theta(t). \qquad\qquad 9)$$

Here the minus sign in the second term is related to the fact that we are considering a radius that decrease as the angle *θ(t)* increase.

From the first relation of constrains (8), we can derive the angular velocity formula for the system:

$$\omega(\theta) = \frac{v_t}{R(\theta)} = \frac{d\theta}{dt}. \qquad\qquad 10)$$

We can use the equation (9) and (10) to make the radius as a time dependent variable:

$$\int v_t dt = \int \left(R_{in} - \frac{D}{4\pi}\theta(t) \right) d\theta$$

$$t = R_{in}\theta(t) - \frac{D}{4\pi}\theta(t)^2$$

that can be resolved as *θ(t)*:

$$\theta(t) = \frac{R_{in} \pm \sqrt{R_{in}^2 - \frac{Dv_t}{2\pi}t}}{D/4\pi}$$

and with the finally substitution in the equation 9), we can find the equation:

$$R(t) = \sqrt{R_{in}^2 - \frac{Dv_t}{2\pi}t} \; . \qquad\qquad 11)$$

From the last equation we can also get the total manoeuvre time considering

$$R(t_{fin}) = \sqrt{R_{in}^2 - \frac{Dv_t}{2\pi}t_{fin}}$$

$$t_{fin} = 2\pi \frac{\left(R_{fin}^2 - R_{in}^2\right)}{Dv_t} \qquad\qquad 12)$$

Considering now, the relationship between the second cardinal law and the angular momentum for a rigid body, we can write the following:

$$\frac{db}{dt} = T^e \qquad\qquad 13)$$

where the T^e is the external torque needed by the system to change its angular momentum. From equation 1), the angular momentum can be also written as a function of the imposed constant tangential velocity and the radius, considered as concentered, of the two telescopes:

$$\frac{db}{dt} = 2Mv_t \frac{dR}{dt}$$

Deriving the previous equation, substituting the function of $R(t)$ as wrote in 11), gives, if compared with the (13), the torque T^e as a function of time:

$$T^e(t) = Mv_t^2 \left(\frac{D}{2\pi\sqrt{R_{in}^2 - \frac{Dv_t}{2\pi}t}} \right) \; . \qquad\qquad 14)$$

Considering a thruster with variable couple, applied to the telescopes of the form $T^e(t) = F^e(t)R(t)$, from the 14) we obtein:

$$F^e(t) = Mv_t^2 \left(\frac{D}{2\pi\left(R_{in}^2 - \frac{Dv_t}{2\pi}t\right)} \right) \qquad\qquad 15)$$

In the following figures are reported the spiral trajectory for a thruster-assisted manoeuvre, and the necessary torque to obtain it
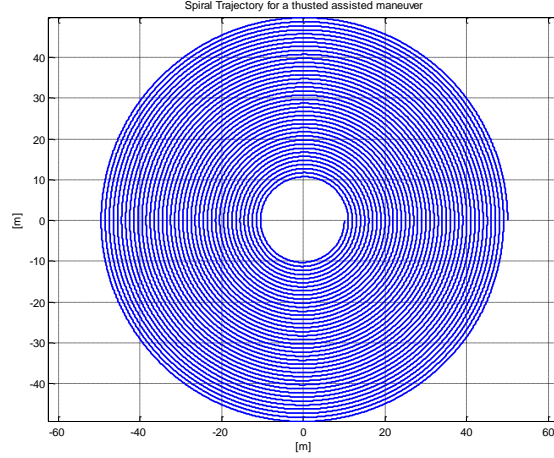
Figure 26. Spiral trajectory for a thrusters assisted manoeuvre.
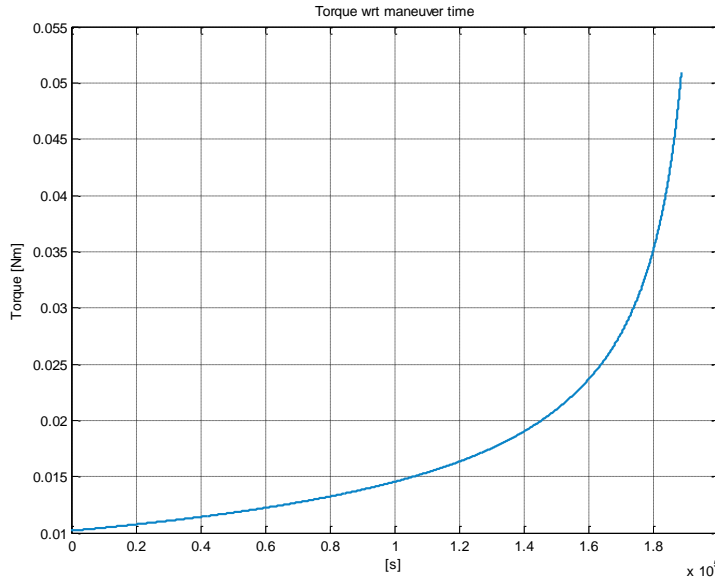
Figure 27. Spiral trajectory for a thrusters assisted manoeuvre, torque vs time

4.4.4   Propellant consumption for the interferometer manoeuvres

The thrust of a rocket engine can be wrote as a function of mass flow rate and the velocity of exhaust gasses: $F^e(t) = \dot{m}v_e = \dot{m}I_{sp}g_0$. Comparing the last equation with the (15) and integrating on the manoeuvre total time, we obtain the total fuel mass needed for the complete manoeuvre:

$$\Delta m = \frac{1}{I_{sp}g_0}\int_0^{t_f} F^e(t)dt = \frac{1}{I_{sp}g_0}\frac{M}{v_t}\ln\left|R_{in}^2 - \frac{Dv_t}{2\pi}t\right|_0^{t_f} \qquad (16)$$

Imposing the following, reasonable, quantities:

M = 1000 kg single telescope mass
v_t = 0.04 m/s
I_{sp} = 330 ÷ 1000 s
R_{in} = 50 m
R_f = 10 m
D = 2 m

we can calculate the total time needed for the observation:

$$t_f = 188495 \text{ s} = 2.18 \text{ days}$$

and mass consumption for the single manoeuvre:

$$\Delta m = 0.994 \text{ Kg} \div 0.328 \text{ Kg}$$

4.5 NOISE ANALYSIS

In this section will be considered the possible causes of perturbations of the observations performed with a FIR space interferometer. In particular the noise perturbing the single spectroscopic measurements of a (u, v) point will be considered, and due to the noise presents on every element of the interferometer (each telescope, hub combiner) and to the differential noise due to the vibration of the whole telescope structure.

The noise concerning the spectroscopic measurements here analysed is strictly connected to the OPD errors (see 2.5.1), or "PISTON effect" considered in the SPIRIT study. This effect, together with the pointing and WFD errors (see 2.5.1), represents the major sources of noise, determining the loss of visibility and spectral and imaging fidelity. Hereafter we analyse the direct effect of these disturbances, acting as jitter during the acquisition of the spectrographic signal as function of the positions of the sled of the OPD.

4.5.1 Analysis of noise relative to the acquisition of a single point of the plane u, v (spectroscopic measurement)

To the analysis of the noise relative to the single point of the (u, v) plane it is necessary to take into account that, as indicated in the ESA CDF FIRI study, the single spectroscopic measurement for a point in the u, v plane is performed in a time of order of about $24\ sec$, for a total number of points in the u, v plane equal to about 1370. Similar numbers are found for SPIRIT. For each elementary measure the base configuration to consider is as shown in the following figure:
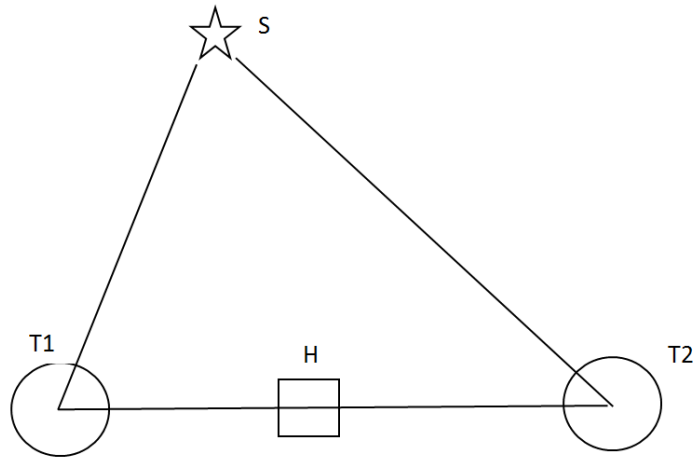
Figure 28. Base interferometer configuration for the measurements of a single u, v point.

where the indicated points are:
S: Position of the observed sky area,
T1: First telescope.
T2: Second telescope
H: Interferometer Hub (Point where the recombination for the execution of interferometry takes place)

The whole system is referred to an inertial reference frame and we can think that the plane defined by the triangle is coplanar with the xy plane of the inertial reference. In this configuration are to be found all the causes of a possible change in the two paths listed below:

$$S - T1 - H \ and \ S - T2 - H,$$

and then the variations of the lengths: $S - T1, \ S - T2, \ T1 - H \ and \ T2 - H$.
These lengths can vary both due to the overall movement of the support structure of the two telescopes and the central hub, both due to the noise present on each single element.
We consider now all types of noise that can act on the single elements (T1, T2, H) in an independent manner and such as to give contributions not correlated with those of the other two units. The types of noise can be of two types:

• Stochastic Noise
• Deterministic Noise.

The first type of noise is associated with vibrations that extend in a certain band of frequencies without showing particular peaks, for which the integration time, determines a narrowing of the band on which this noise is integrated with a consequent decrease of its *rms* values. The noises of this type, associated with different sources are *added quadratically*.
The second type of noise is associated with vibrations and signals present at precise frequencies, for which the integration produces a narrowing of the frequency band in

which the noise is integrated, but if this band includes the frequency of the deterministic noise, the latter is not reduced. In this case the noises are *added linearly*.

For both types of noise it is necessary to assess their effect on the interferometric measurement and thus give the requirements for the maximum acceptable noise or determine them with precision and remove their effect in the process of data analysis.

Only for the noise of the deterministic type, one can think to measure them with a suitable system, for example with an accelerometer and use this information for controlling the actuators that cancel the effect. Since the noise is added to the signal, it is necessary to actuate the feedback only at frequencies in which the noise is present, while the system should be free at frequencies in which the signal acts. In this case all the differential movements of the interferometer elements can be considered as noise.

Both types of noise, stochastic and deterministic, act to change the difference of the two optical paths, producing a variation of the interference of the two light beams at the detector, with an intensity that varies with the period of the wavelengths present in the beam, we would refer to this as the *jitter effect*.

Recalling that the spectroscopic scanning is obtained with the movement of the slide of the OPD and taking into account that the minimum wavelength to be detected is equal to $\lambda_{min} = 25\ \mu m$, it is clear that the effects of noise, translated into displacement, must be much smaller than this minimum wavelength.

One may think that the displacements of the OPD slide determine a linear variation of the optical path in a ratio one to one, or through a certain multiplication factor (multiple reflections), in any case, the time required to produce this variation determines, in its inverse, the frequency at which the intensity modulation is seen.

$$I = I(\lambda) = I(v \cdot t) = I(v_s/f))$$

The criteria for choosing the sled velocity are:
1) Minimization of the acquisition time of the single point of the u, v plane
2) Transferring the Signal to a frequency range where vibrational noise is low.

In the hypothesis of a movement of the slide at constant speed v, the peaks of maximum intensity will occur at times equal to $t_n = \frac{\lambda_n}{v}$ and then at frequencies $f_n = \frac{v}{\lambda_n}$; the highest frequency will correspond to the minimum wavelength, assumed to be $\lambda_{min} = 25\ \mu m$. It is therefore important to make a frequency analysis of the noise present on the satellite and then choose a suitable speed of the slide such as to send the signals to be detected, in a frequency band in which the vibrational noise level is minimal.

The problem is thus to acquire a signal that varies with λ, as function of time through the speed of the sled. The presence of noise causes acquisitions not to be made at well-determined positions as expected from the constant speed of the slide but in positions determined by this velocity plus a noise contribution. In other words the problem is thus to acquire a signal as a function of λ where λ does not vary linearly but has components due to noise. It follows that:

$$I = I(\lambda) = I(v \cdot t + \lambda_r)$$

In case the considered spectral band of the FIR interferometer is as below:
$$[\lambda_{min}, \lambda_{max}] = [25\ \mu m, 500\mu m]$$

and if it is decided that the max distance, related to the largest wavelength is performed by the ODL in ~26 s, it follows a speed equal to: $V_S = 500 \cdot \frac{10^{-6}}{26} = 1.9 \cdot 10^{-5}$m/s. The consequent frequency band in which the signals are translated is:

$$[f_{max}, f_{min}] = \left[\frac{V_s}{\lambda_{min}}, V_s/\lambda_{max}\right] = [6.4 \cdot 10^{-1}\text{Hz}, 3.8 \cdot 10^{-2}\text{Hz}]$$

Here below a simulation is reported concerning the acquisition of an interferometric signal $I = I(\lambda)$, in the presence of the indicated jitter noise. In the first analysis we considered the acquisition of an interferometric signal varying sinusoidally with respect to λ, acquired through a constant speed movement of the OPD, with added white noise.

$$I(\lambda) = I_0 \cdot \cos\left(2 \cdot \pi/L_s \cdot (V_0 \cdot t + x_b)\right)$$

It is necessary to note that this case is not corresponding to a real case, because usually the Brownian noise is in terms of force or acceleration and the corresponding displacements is obtained integrating it and so decreasing with 40dB per decade with respect to the accelerations, nevertheless the example give good indications of the limitations that the jitter effects introduce in the spectroscopic measurements.
In Figure 29 the results of this simulation are reported using the parameters reported in Table 4.

Table 4. Parameter used for the performed simulation.

I_0	10^{-6}
L_0	$500 \ \mu m$
t_0	$26 \ s$
$V_0 = L_0/t_0$	$1.9 \cdot 10^{-5} \ m/s$
L_s	$1/5 \cdot 10^4 = 20 \cdot 10^{-6}$
x_b	$10^{-6} \frac{m}{\sqrt{Hz}} - 10^{-11} \ m/\sqrt{Hz}$ -

In Figure 30 the analogue simulation is reported obtained changing only the value of the amplitude of signal to be acquired, now equal to 10^{-4} instead of 10^{-6}. It is possible to see that there is no change in terms of ratio between signals to noise.
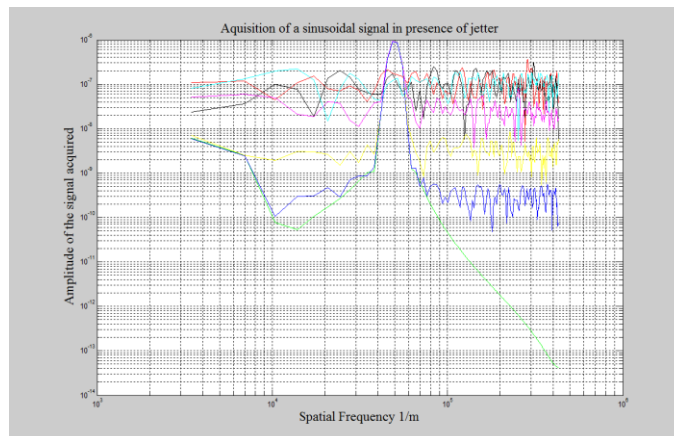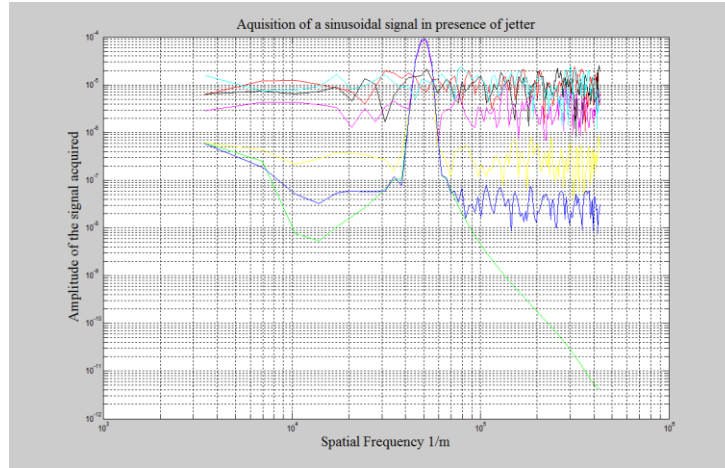
Figure 30. Results of a simulation relative to the acquisition of an interferometric signal considered as simple sinusoid, in the case of the parameter reported in Table 4 except for the value of the amplitude of the signal to be acquired, now equal to 10^{-4} . The level of white noise considered for the displacement is as in Figure 29.

It is possible to deduce that the sinusoidal signal can be detected only if the white noise in displacement is under $10^{-8}\ m/(Hz)^{1/2}$, this to be compared with the spatial frequency to be detected $f_s = \frac{1}{5 \cdot 10^4}$, corresponding to $\lambda_s = 20\ \mu m$.

If we are in the presence of a deterministic noise at a certain frequency, always in the case of the above example, the amplitude of the signal to be detected would be given by the relation:

$$I = I_0 \cdot cos\left(\frac{2 \cdot \pi}{\lambda_0}(v \cdot t + v_0 \cdot t_0 \cdot cos(\omega_0 t))\right)$$

4.5.2   Example of noise presents on a satellite.

Here an example of vibrational noise that can be present on a satellite is described. The information corresponds to that of the Radio Science Experiments on the ESA Cornerstone mission to Mercury, BepiColombo.

In Table 5 the requirements for the deterministic vibrational noise inside the frequency measurements band on board the MPO (Mercury Planetary Orbiter) are shown, one of the two satellite considered for the BepiColombo Mission for the exploration of Mercury and to test the General Relativity; requirements that hold in the context of the RSE (Radio Science

Experiments). The corresponding displacements values can be found using the relation: x = a/(2 * pi * f)^2. In Table 6 we show the requirements for the stochastic vibrational noise inside the frequency measurements band.

Table 5. Vibrational noise inside the frequency measurements band on board the MPO (Mercury Planetary Orbiter) BepiColombo Mission for the RSE (Radio Science Experiments).

Frequency Hz	$3 \cdot 10^{-5}$	$10^{-4} - 10^{-3}$	10^{-1}
Acceleration values (m/s²)	$3 \cdot 10^{-9}$	$10^{-9} - 10^{-9}$	10^{-8}
Corresponding displacements m	$8.4 \cdot 10^{-2}$	$2.5 \cdot 10^{-3} - 2.5 \cdot 10^{-5}$	$2.5 \cdot 10^{-8}$

Table 6. Stochastic vibrational noise inside the frequency measurements band on board the MPO (Mercury Planetary Orbiter) BepiColombo Mission for the RSE (Radio Science Experiments)

Frequency Hz	$3 \cdot 10^{-5}$	$10^{-4} - 10^{-3}$	10^{-1}
Acceleration values ($^{m/s^2}/_{\sqrt{Hz}}$)	$3 \cdot 10^{-9}$	$10^{-9} - 10^{-9}$	10^{-8}
Corresponding displacements $^{m}/_{\sqrt{Hz}}$	$8.4 \cdot 10^{-2}$	$2.5 \cdot 10^{-3} - 2.5 \cdot 10^{-5}$	$2.5 \cdot 10^{-8}$

In Figure 31 the requirements of Table 5 are illustrated, showing that the acceleration values in black and displacements in red, and in Figure 32 is shown the requirements for the microvibration deterministic noise outside the frequency measurements band on board the MPO (Mercury Planetary Orbiter).
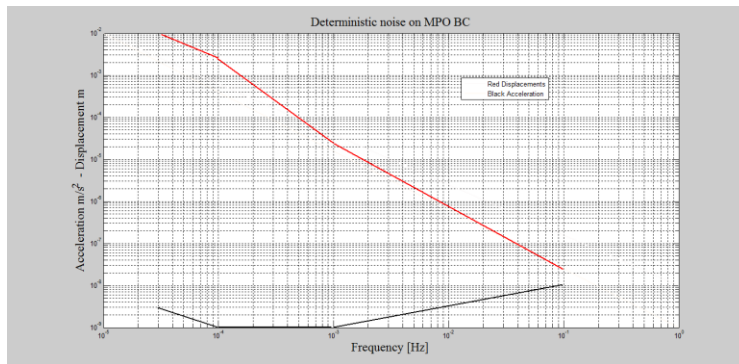
Figure 31. Deterministic vibrational noise inside the frequency measurements band on board the MPO (Mercury Planetary Orbiter) BepiColombo Mission for the RSE (Radio Science Experiments).
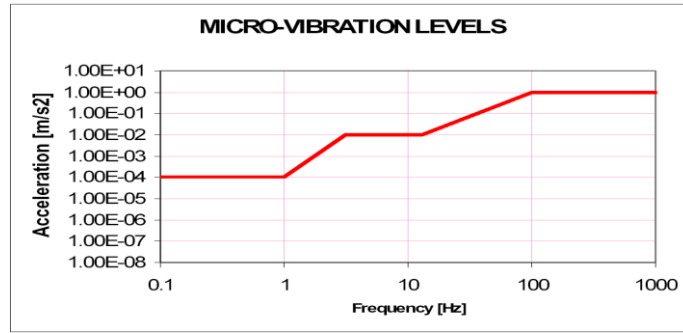
Figure 32. Level of the micro-vibration deterministic noise outside the frequency measurements band on board the MPO (Mercury Planetary Orbiter), takes as requirement.

In Figure 33 and Figure 34 the noise presents on the MPO BepiColombo due to the motions of the solar array and the HGA (High Gain Antenna) respectively are shown, as assessed by ASTRIUM (ASTRIUM ASSESSMENT OF THE MICROVIBRATION BUDGET FOR BepiColombo).
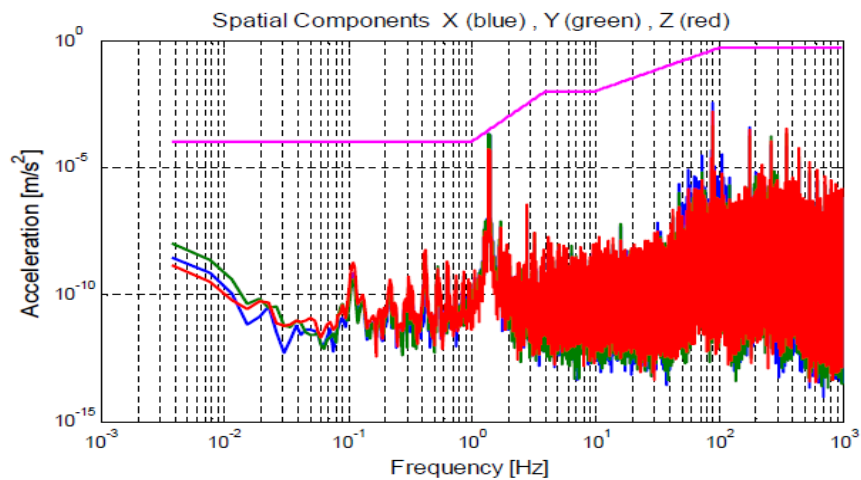
Figure 33. Noise presents on the MPO BepiColombo due to the motions of the solar array as assessed by ASTRIUM (ASTRIUM ASSESSMENT OF THE MICROVIBRATION BUDGET FOR BepiColombo).
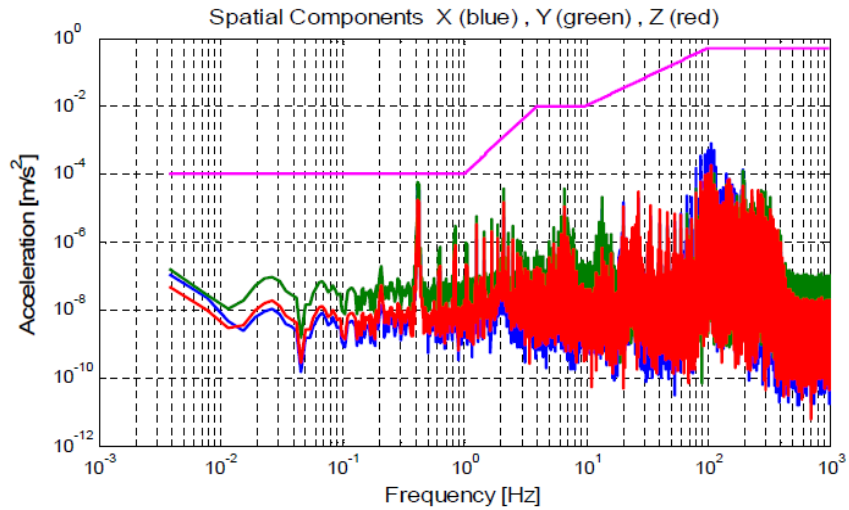
Figure 34. Noise presents on the MPO BepiColombo due to the motions of the HGA (High Gain Antenna) as assessed by ASTRIUM (ASTRIUM ASSESSMENT OF THE MICROVIBRATION BUDGET FOR BepiColombo).

Figure 35 shows the micro-vibration noise on board the MPO outside the frequency band in x and z direction due to the reactions wheels, compared with the requirements (solid line). The translation between accelerations and displacements can be performed as previous indicated (double integration)
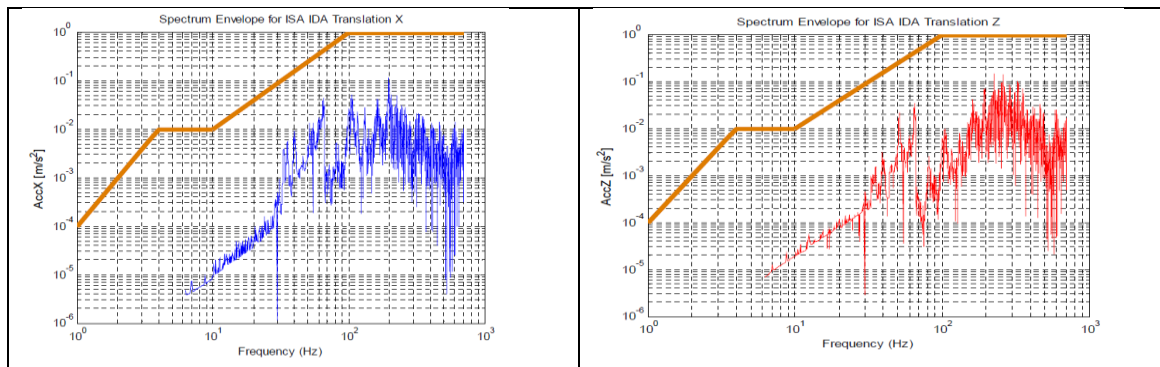
Figure 35. Micro-vibration noise on board the MPO outside the frequency band in x and z direction due to the reactions Wheels, compared with the requirements (solid line). The translation between accelerations and displacements can be performed as previous indicated (double integration).

In Figure 36 the spectral density is shown of the solar radiation pressure for the BepiColombo MPO in orbit around Mercury, very close to the Sun. The solar radiation pressure at the orbital period of the MPO is $10^{-6} \, m/s^2$, corresponding to a displacement equal to 1.6 m at the orbital period of $2.3h$.
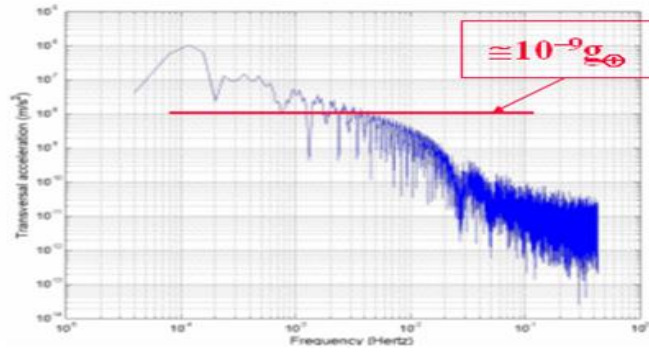
Figure 36. Spectral density of the solar radiation pressure for the BepiColombo MPO in orbit around Mercury and for the transversal acceleration component.

The MPO IMU mission uses an accelerometer to measure the on-board accelerations. The accelerometer measurements error is connected to its position vs the MPO COM, position that can be defined with a vector indicating the distance between the instantaneous MPO center of mass (CoM) and that of the accelerometer CoM:

$$\vec{R} = \vec{R}_0 + \Delta\vec{R}_0 + \vec{R}_t(t) + \Delta\vec{R}_t(t)$$,

given in terms of time-independent and time-dependent parts (known parts and error parts). In Table 7 is reported the angular rate and angular acceleration noise requirements for an accelerometer used for the MPO IMU navigation in case it is installed with its CoG coincident with the MPO COM (case A) and at a distance of 20cm (case B).

Table 7. Accelerometer requirements on the angular rate and angular acceleration

	Case A)	Case B)
$\delta\omega$	$1.34 \cdot 10^{-5} \quad rad/s/\sqrt{Hz}$	$0.54 \cdot 10^{-5} \quad rad/s/\sqrt{Hz}$
$\delta\dot{\omega}$	$1.76 \cdot 10^{-8} \quad rad/s^2/\sqrt{Hz}$	$0.56 \cdot 10^{-8} \quad rad/s^2/\sqrt{Hz}$

In the table8 the MPO temperature variations at the orbital period are reported, sidereal period, and that due to random fluctuations. It is clear that the temperature variation will be much less for the interferometer in L2, nevertheless considering the big dimension of the satellite their influence due to thermal contraction will be high especially at the interferometer angular rate.

Table 8. MPO temperature variations at the orbital period, sidereal period, and random.

Frequency	T (°C)
Mercury revolution period	25 peak-peak
MPO orbital period	4 °C peak-peak
Random noise	$4 \; °C/\sqrt{Hz}$

At the end of this section we like to remember that the FIRI frequency band, in which we will see the signal, is:

Band: $[f_{max} \ f_{min}] = [V_s/\lambda_{min} \ V_s/\lambda_{max}] = [6.4 \cdot 10^{-1}\text{Hz} \quad 3.8 \cdot 10^{-2}\text{Hz}]$.

Assuming that the optical path delay slide needed for a R~3000 we obtain, $MPD_{max} = 6.5 \ cm = \ 0.065 \ \cdot 10^{-3} \ m$, in a time of 26 s, it follows that its speed is equal to:

$$v = \frac{6.5 \cdot 10^{-2}}{26} = 2.5 \cdot 10^{-3} \ m/s$$

At this speed correspond a $f_{min} \ ed \ f_{max}$ of the signal to be detected respectively equal to

$$f_{min} = \frac{v}{\lambda_{max}} = \frac{2.5 \cdot 10^{-3}}{500 \cdot 10^{-6}} = 5 \ Hz$$

$$f_{max} = \frac{v}{\lambda_{min}} = \frac{2.5 \cdot 10^{-3}}{20 \cdot 10^{-6}} = 125 \ Hz$$

It is difficult to work at these frequencies due to the high value of the noise present on the satellite. In order to reduce the frequency of the signal to be detected, it necessary to work with a speed of the slide a factor of 10 or 100 lower.

4.5.3 Analysis of noise relative to the acquisition of all points in the u, v plane (spatial measurement)

The reconstruction of the mapping of the sky area inside the FOV is made by means of inverse Fourier transform of all spatial frequencies with their proper amplitudes, contained in the u, v plane, measured with the interferometer for all appropriate radial and angular positions of the two telescopes. In the case of FIRI the u, v plane can be decomposed of 1373 distinct points (that fill it densely) and as mentioned earlier each point is observed by the appropriate spectroscopic scanning for a time of ~26 sec and then proceeding to the next measurement by moving the two telescopes (in radial and angular manner) with respect to the line joining the HUB with the center of the FOV.

But, in every case the angular resolution is determined as function of wavelength λ and baseline B by the relation $\alpha = \frac{\lambda}{2B}$. At the maximum baseline observation, every point is acquired during a displacement of 1m with a radius of rotation equal to 50m, and so the average angle associated to this point and related to the requirement precision in angle is about $\frac{1}{50} rad$ which is not very stringent.

In the following the list of the main causes of noise to be considered for the evaluation of the deterministic and stochastic noises acting on the interferometer are reported; the list holds for the noise in the whole structure of the interferometer as well as on each of its elements (hub and telescope)

List of the deterministic noise effects
1) Inertial accelerations ω, $\dot{\omega}$
2) Attitude Control
3) Gravity Gradient
4) Vibrational noise due to the AOCS
5) Vibrational noise connected to the satellite structure
6) Thermal noise
    - Solar Radiation pressure (Satellite rotation)
    - Noise due to the power dissipation of the instruments presents on the satellite (principally On Off of the instruments)
7) Noise due to the appendices movements.
    - Solar pannel
    - RW vibrations (desaturation, maneuvers)
    - Antenna movements.
8) Sloshing fuel
9) Out of band Microvibration (High frequency)

List of the stochastic noise effects
1) Inertial accelerations $\delta\omega$, $\delta\dot{\omega}, R, \Delta R$
2) Gravity Gradient $R, \Delta R$
3) Vibrational noise due to the AOCS
4) Vibrational noise connected to the satellite structure
5) Thermal noise
    - Solar Radiation pressure (Satellite rotation)
    - Noise due to the power dissipation of the instruments presents on the satellite (principally On Off of the instruments)
6) Noise due to the appendices movements.
    - Solar pannel
    - RW vibrations (desaturation, maneuvers)
    - Antenna mouvements.
10) Sloshing fuel

4.6 MODAL ANALYSIS SIMULATION FOR A CONNECTED INTERFEROMETER

In this section we present a modal analysis concerning an interferometer constituted of two telescope connected to a central hub by means of two mechanical booms. In Table 9 are reported the main parameter used in the simulation.

Table 9. List of the main parameter used in the modal analysis

	Value
Satellites Mass (kg)	2 X 850
Central Hub Mass (Kg)	313
Booms Mass (Kg)	2 X 421
Booms length (m)	2x50

Figure 37 shows the assembly of the interferometer with the two telescope and the central hub used in the following simulations, and Figure 38 shows the individual parts, telescope, boom, and hub. Note that in this first analysis the values for the components used in the simulation are taken from the FIRI study, in particular for what concern the structure of the boom.

14,680m
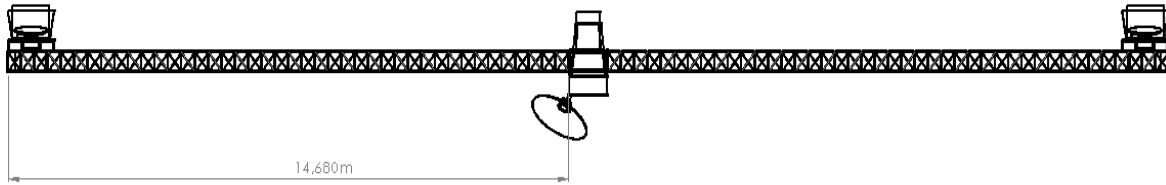
Figure 37. Assembly of the interferometer with the two telescope and the central hub.
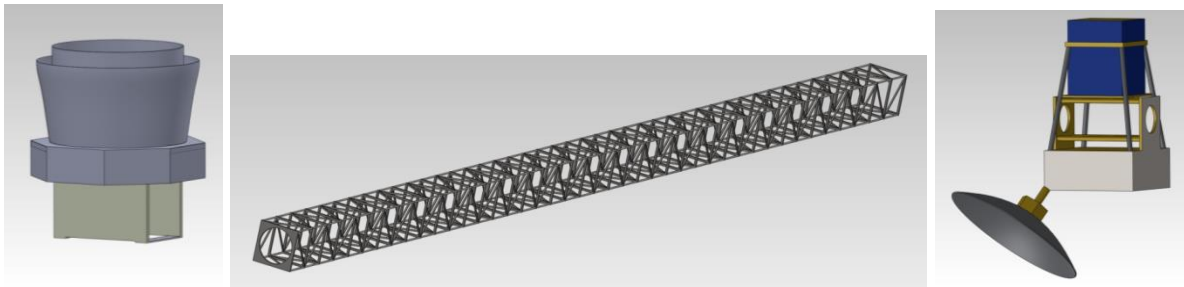
Figure 38. Model design of telescope (left), boom (middle), and hub (right).

Table 10 reports the frequencies obtained with the modal analysis for the first four normal modes, illustrated in Figure 39.

Table 10. First fourth frequencies obtained with the modal analysis

Normal Mode	Value (Hz)
First	0,84
Second	0,098
Third	3,39
Fourth	3,5
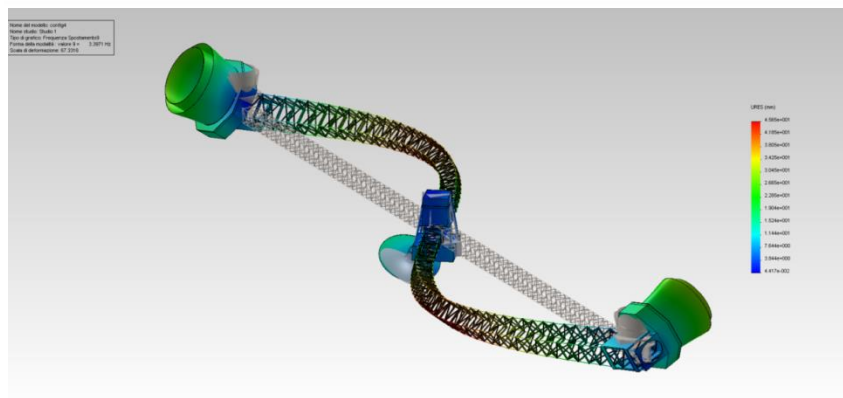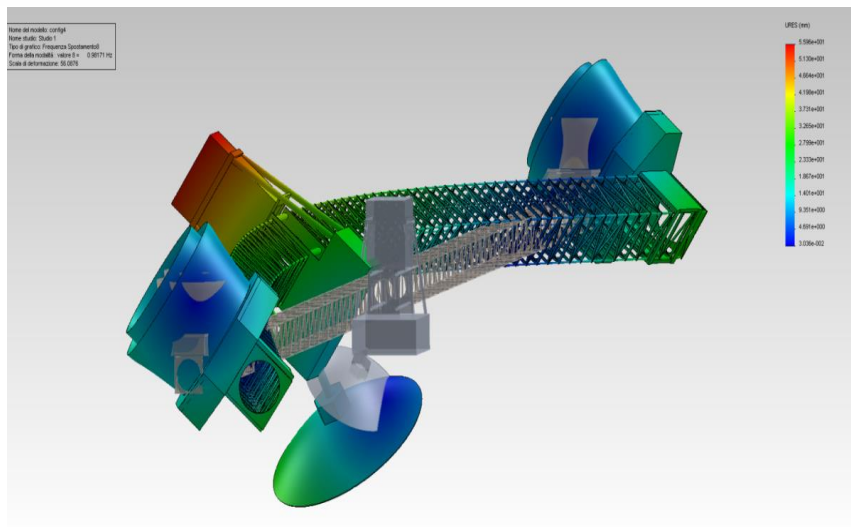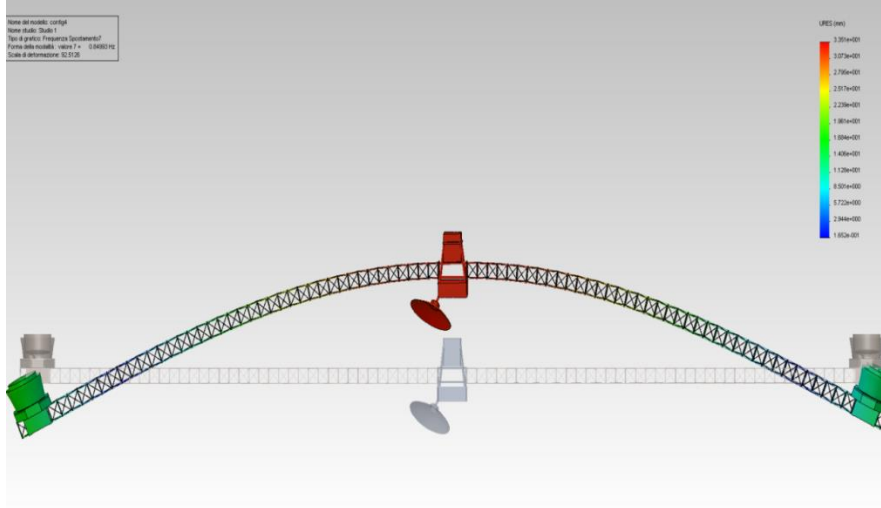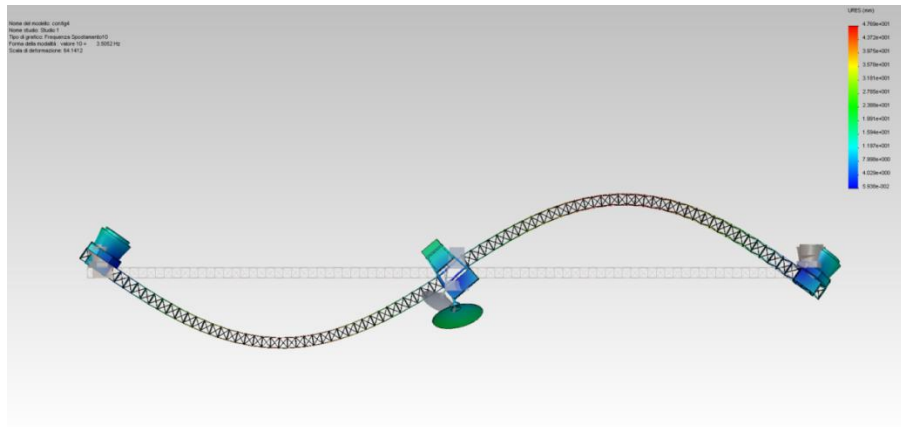
Figure 39. From top to bottom, visualization of the first four normal mode of the FIRI structure.

The analysis presented is of fundamental importance because it allows to determine the indicative values of the frequencies of the structure and in particular the shape of the vibrational mode of the system, that attain to the metrological problem in terms of precision in the distances between each telescope and the central Hub, but also in the pointing precision of each telescope to the source. In particular the indicated normal modes are excited by transient effects induced by the manoeuvres of the telescope (retargeting and change of the ITD), and it's of fundamental importance to evaluate their values and to introduce dissipaters able to reduce their relative mechanical values so to come back after the induced transient to a low level of vibration. In the following section a dynamical analysis will be presented concerning the first normal mode of the interferometer, here introduced.

4.7   DYNAMIC ANALYSIS IN CLOSED LOOP OPERATION

In the following section the dynamic analysis of the interferometer using thrusters to maintain constant angular velocity during the entire u-v plane scan is reported.

4.7.1   Simulations

The study starts with a dynamical analysis performed using the *Simmechanics* tool of MATLAB, this analysis is a continuation of the modal analysis performed in the previous section and gives the ideas on the dynamic vibration of the interferometer and on the possible control loop to be implemented in order to control its dynamics during the observation.

The tool permits to simulate the dynamics of the bodies through the definitions of the masses, momentum of inertia, their positions, the mechanical constraints (springs), forces and momentum acting on them. The analysis taks as reference the structure shown in Figure 37. In Figure 40 we show the implemented scheme for the performed dynamic analysis.
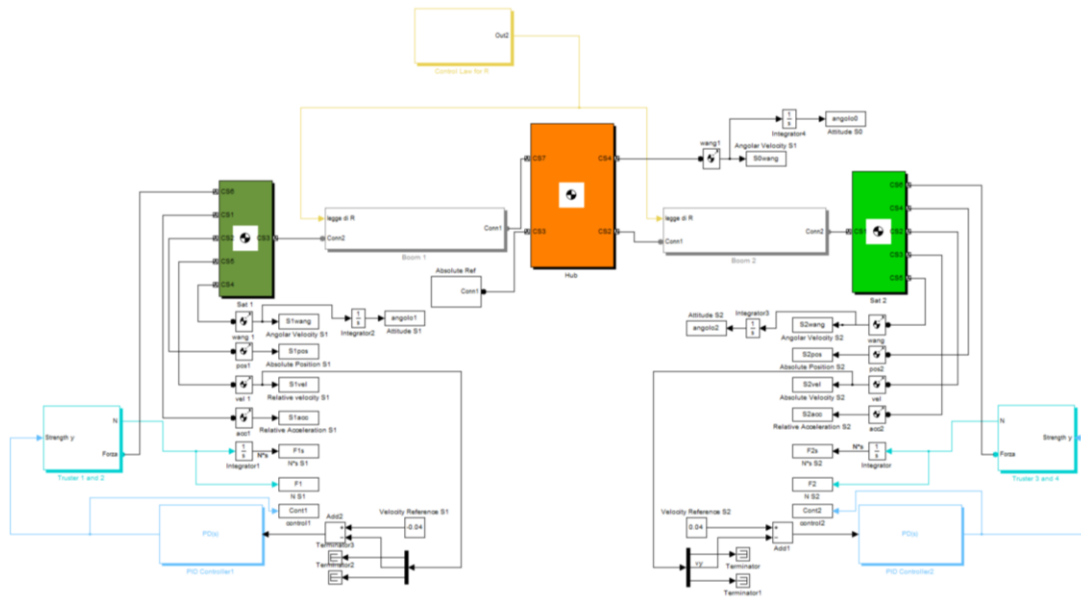
Figure 40. Schematic of the performed dynamic analysis.

The main elements used for this simulation are indicated as extracts of Figure 40, and reported in the following list:

a) Green boxes – Satellites with masses equal to 1000Kg

b) Orange box – Hub with mass equal to 320Kg

c) Two rigid elements with zero mass, connecting the central Hub to the telescopes.

d) Pivot point on the three masses. The introduced elastic torsional spring with the introduced dissipations are defined in order to determinate an oscillation frequency equal to $\omega_{int\_1} = 0.2 Hz$ and a quality factor $Q_1 = 100$, as indicated in the FIRI study where its values range between 20 and 200.

e) Yellow box – Radial actuator with possibility to contain the law for the ITD (Inter Telescope Distance) change: 1m steps, spiral ecc.

f) Blue boxes – Two actuators (thrusters) and two PID (Proportional Integral and Derivative) for the control loop actuation.

g) Comparing elements to determinate the desired tangential velocity, taken equal to $0,04 \ m/s^2$.

h) All the analysis is performed in a two dimensional case (on the rotational plane)

The indicated parameters are summarized in Table 11.
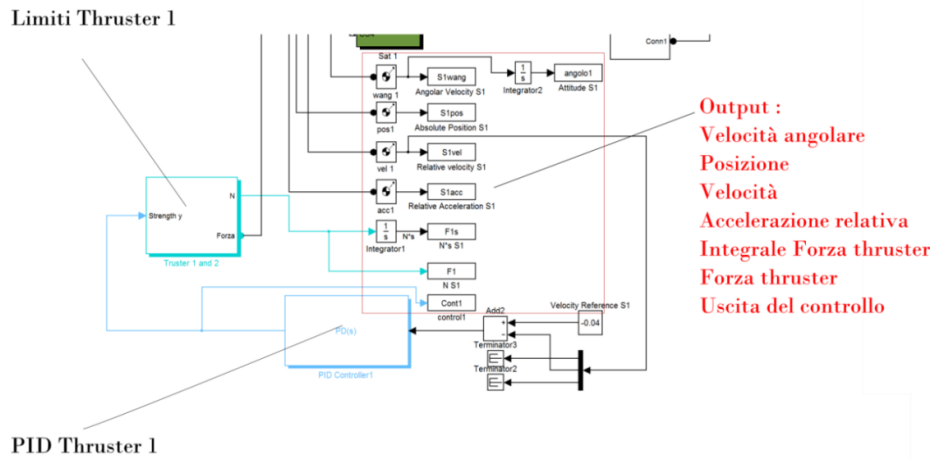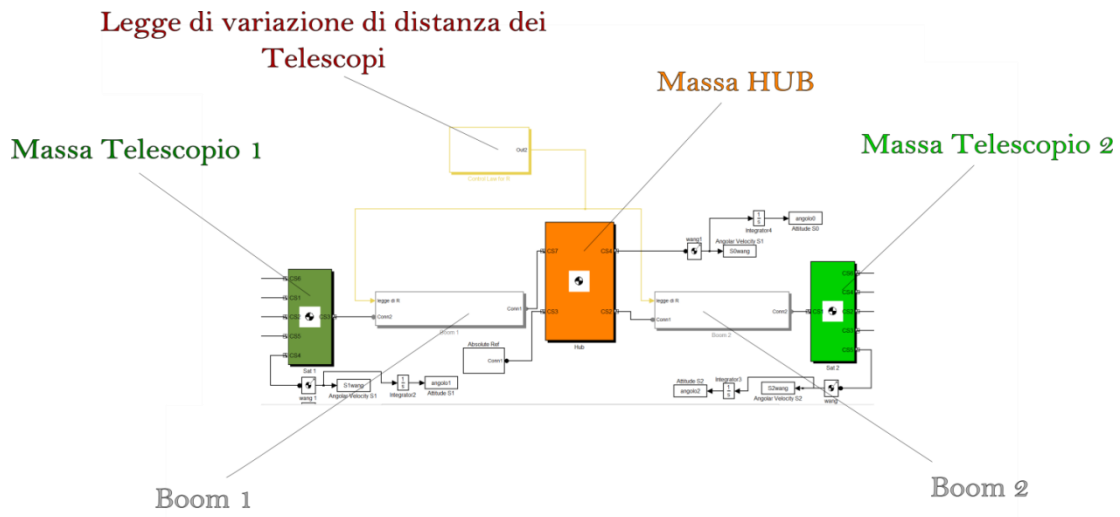
Figure 41. Extracts of Figure 40 naming the main elements used for the simulation.

Table 11. List of the main parameters and condition used in the dynamic analysis

	Value
Satellites Mass (kg)	2 X 1000
Central Hub Mass (Kg)	320
Booms Mass (Kg)	2 X 0
Booms length (m)	2X50

Figure 42 reports the analog analysis performed for FIRI, with the evidence of the dissipation factor.
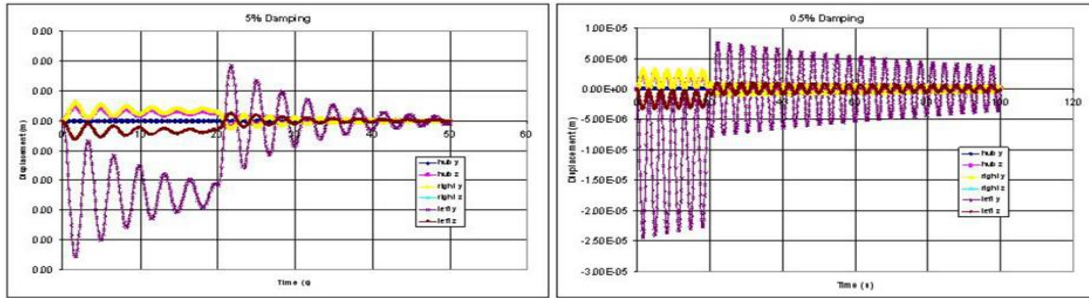
Figure 42. Analysis performed for FIRI, with the evidence of the dissipation factor for the transient response of the telescope deceleration for 5% and 0,5% of critical damping.

In the following the results of the performed analysis are shown. The two telescopes are initially positioned at $50m$ away from the HUB, the system will be posed in rotation with a tangential velocity equal to $v_T = \omega \cdot \frac{ITD}{2} = 0{,}04 \ m/s^2$, in this case, with $ITD = 100m$, the interferometer rotates at an angular velocity equal to $\omega = 8 \cdot 10^{-4} \ rad/s$; after a rotation of $180°$ the ITD will be reduced of $1m$ applying to the telescope a radial acceleration of sinusoidal shape for a time of $20s$. This radial acceleration besides the reduction of the ITD, produces also a transient in the interferometer that will be damped with a time constant equal to $\tau = Q_1/\omega_{int\_1}$. Remembering that ω_{int_1} is the angular velocity of the first interferometer normal mode, after every $180°$ of rotation the procedure is repeated.

When the ITD is changed due to the momentum conservation law, the angular velocity increases. The thrusters can act to keep it at the assigned value by means of a control loop so that the tangential velocity will remain at a constant value equal to $0.04m/s$. We assume the two thrusters are able to give a force equal to $\mp 2.5 \ 10^{-2}N$ with the loop gain fixed at 1000. The control system and the kind of thrusters determine the time and modality of the control.

4.7.2 Trajectory description

In Figure 43 the distance between one telescope and the HUB as function of time is shown during the whole procedure that brings the two telescope to a $ITD = 24m$.
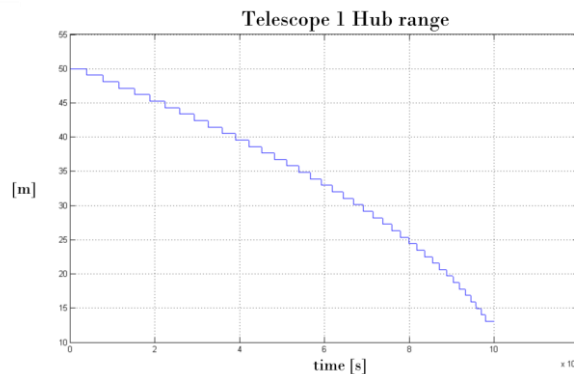
Figure 43. Distance between one telescope ad the HUB vs the time, during the whole procedure that brings the two telescopes to ITD=24m.

In 44 the position of the telescopes is shown as they rotate around the ILS in an inertial reference frame and in the plane perpendicular to the ILS, describing their trajectories during the whole procedure that brings the two telescope to $ITD = 24m$.
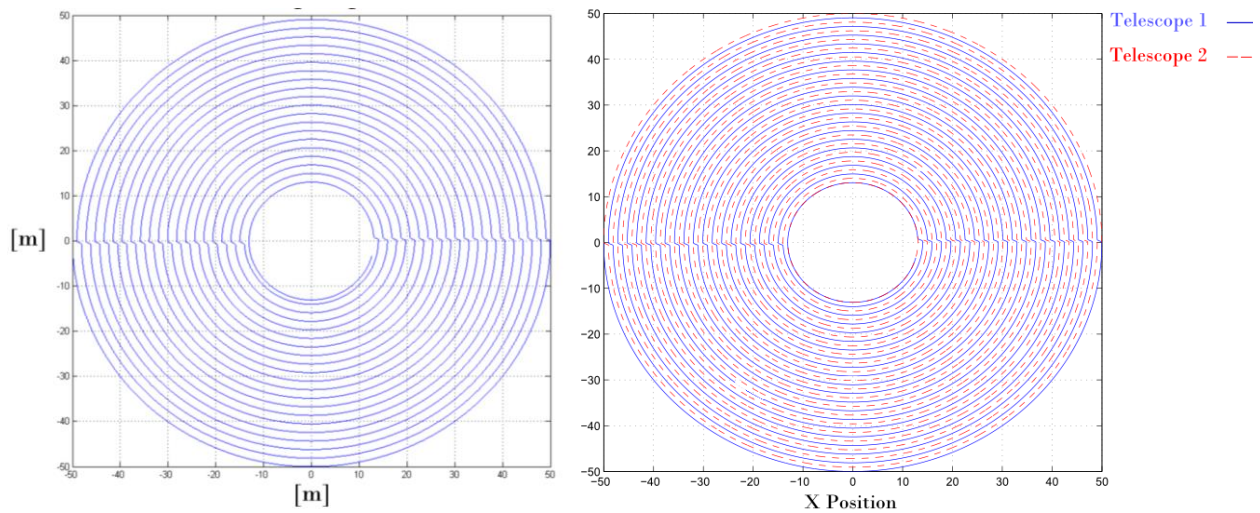
Figure 44. Position of Telescope 1 (left) and both telescopes (right) that rotate around the ILS in an inertial reference frame and in the plane perpendicular to the ILS, during the procedure to acquire the whole u, v plane.

Concentrating on the transient movements during the 1-m change of radial distance at each 180 degree position, Figure 45 shows the trajectory of one telescope in an inertial reference frame and in the plane perpendicular to the ILS during this phase change. Figure 46 shows tangential velocity during this phase change, coming back to the assigned velocity of $0,04 \ m/s^2$ controlled by the control loop. Figure 47 shows the tangential velocity during the entire radial scan.

Figure 48 shows the radial acceleration needed for one telescope to come back to the assigned velocity of $0,04 \ m/s^2$ controlled by the control loop, and Figure 49 and Figure 50 show the temporal evolution of radial position and accelerations and tangential velocity and acceleration, in full scales and zoomed scales, respectively.

Telescope 1 position
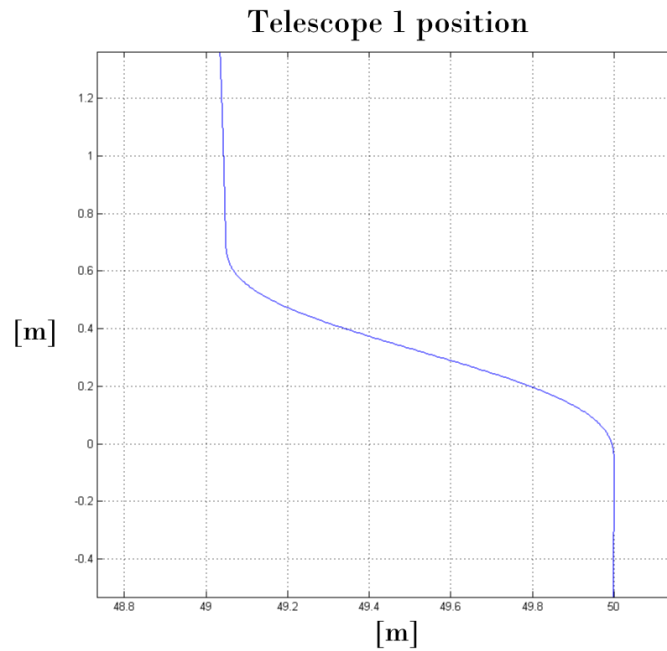
Figure 45. Position of one telescope in an inertial reference frame and in the plane perpendicular to the ILS, describing its trajectory during the phase to change its radial position of 1 m.

Tangential velocity

Start of the radial

Start of the tangential action
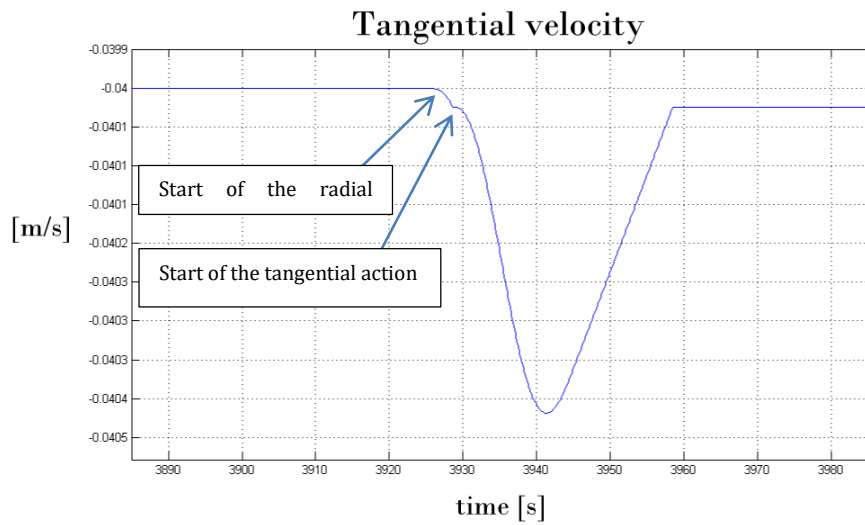
Figure 46. Tangential velocity of one telescope in an inertial reference frame and in the plane perpendicular to the ILS, the tangential velocity increase describing the ITD change phase, to come bake to the assigned velocity of 0,04 m/s controlled by the control loop.
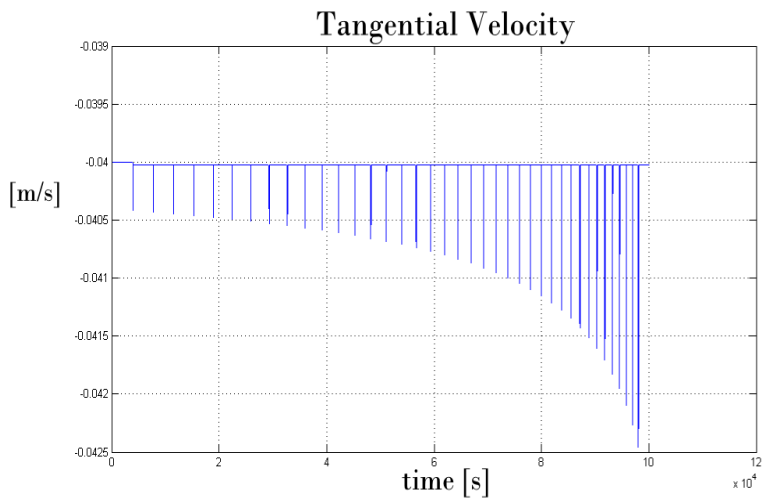
Figure 47. Same as Figure 46, covering the duration of a radial scan.
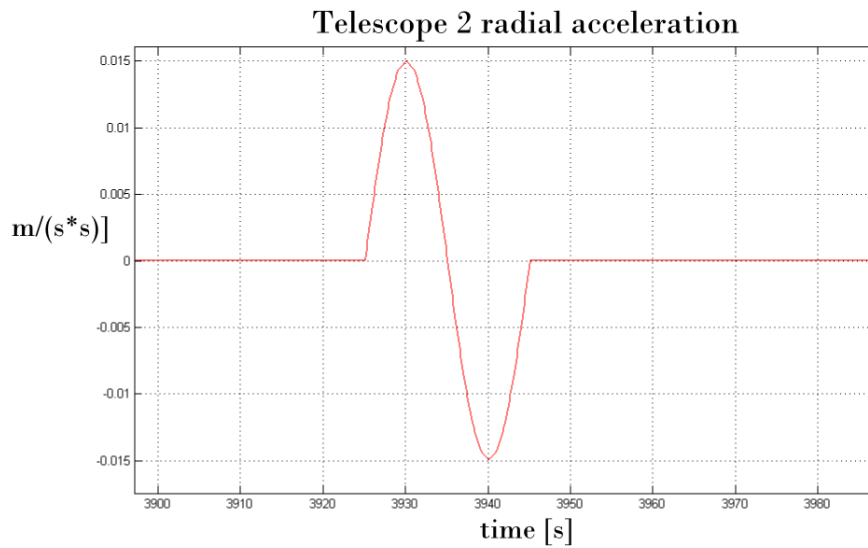
Figure 48. Particular of the radial acceleration of one telescope in an inertial reference frame and in the plane perpendicular to the ILS, describing the ITD change phase, to come bake to the assigned velocity of 0,04 m/s^2 controlled by the control loop.

Figure 49. Graphs showing particulars of some physical quantities, describing the ITD change phase, to come back to the assigned velocity of 0,04 m/s^2 controlled by the control loop.
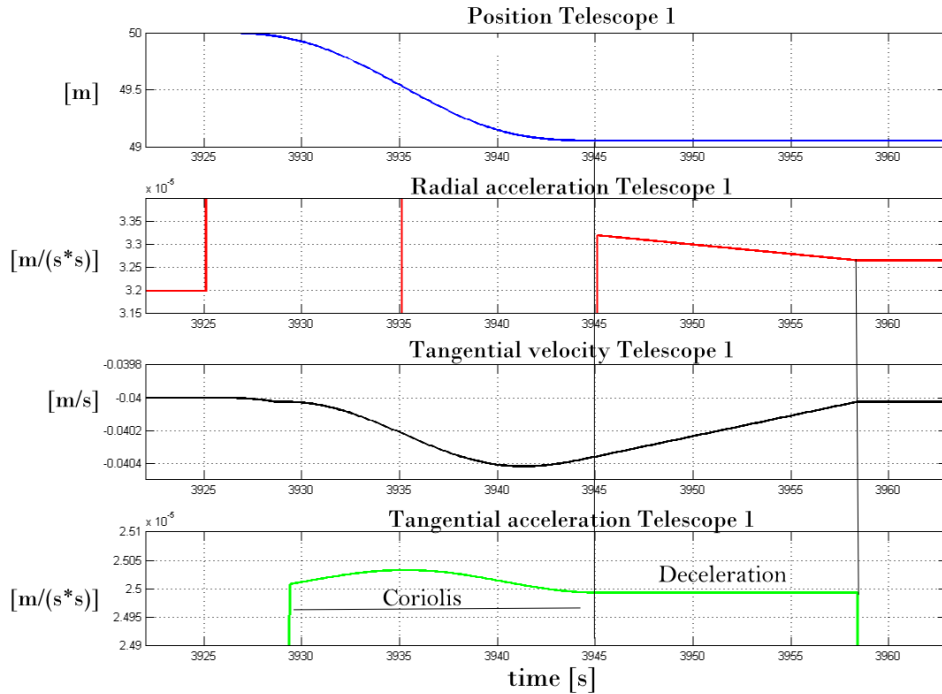
Figure 50. Same as Figure 49 with zoomed vertical scales.

4.7.3   Thruster power

Figure 51 shows the action of the two thrusters during all the observation time to cover all the u, v plane (left) and a zoom on one of the phase change (right). The integrated thruster force is shown in Figure 52, and the resulting change in angular momentum is shown in Figure 53.
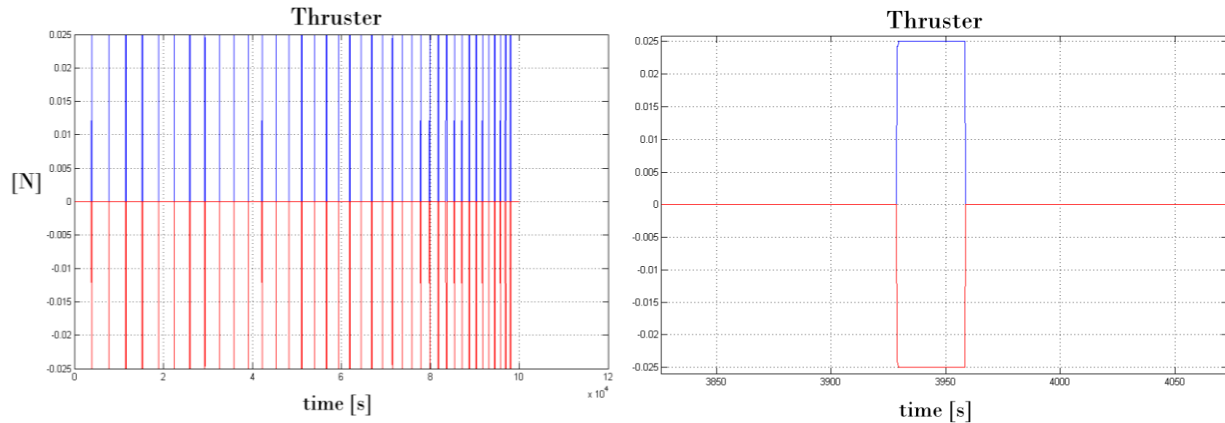
Figure 51. Action of the two thrusters during all the observation time to cover all the u, v plane (left) and during an ITD phase change (right).
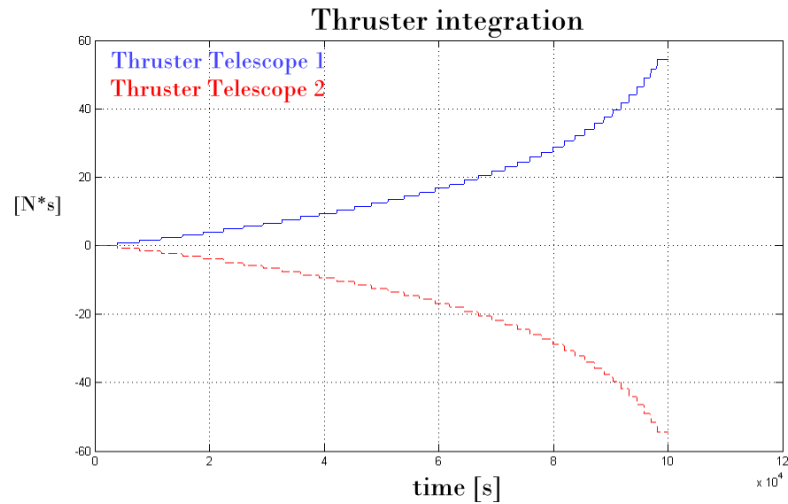
Figure 52. Thruster forces integration action during the whole observation period.
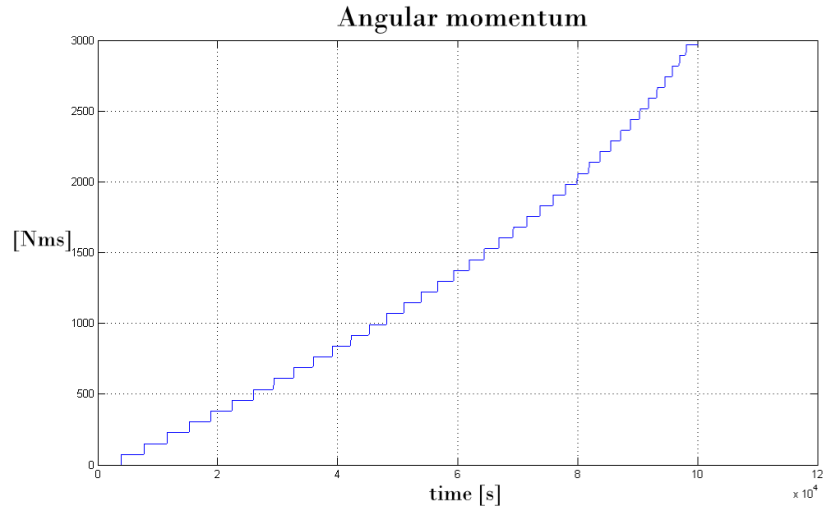
Figure 53. Angular momentum change in the same time of the previous graph.

4.7.4 Transient movements

Transient acceleration and displacements are shown in Figure 54 and Figure 55, respectively. Oscillations of peak-to-peak amplitude of 2 10^{-6}g at a frequency of 0.2Hz, resulting in a displacement of 10 microns, are observed.
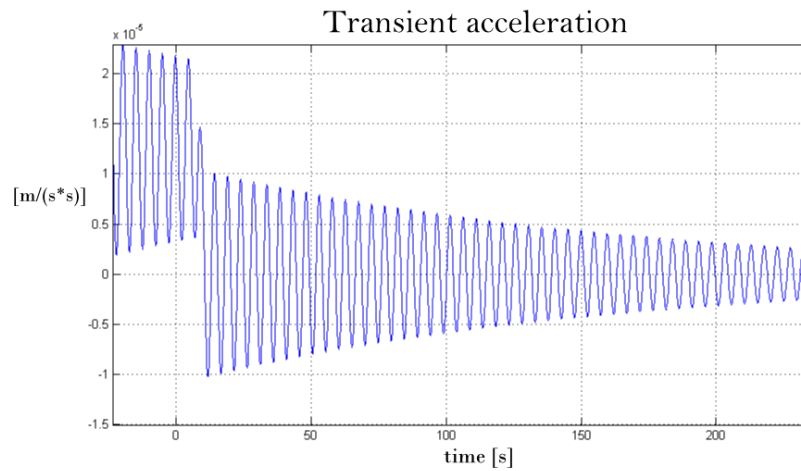
Figure 54. Transient response in acceleration of each single telescope, after the shutting off the thrusters. The full vertical scale is 40μm/s² or 4 10^{-6}g.
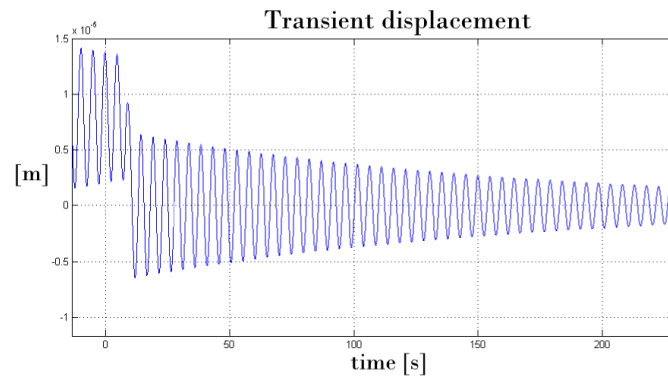
Figure 55. Transient response in displacement of each single telescope, after the shutting off the thrusters. The full vertical scale is 30microns.

5 REFERENCES

[1] "ESA pointing error engineering handbook", http://peet.estec.esa.int/files/ESSB-HB-E-003-Issue1(19July2011).pdf

[2] FISICA deliverable D1.2

[3] Lorenzini, Enrico; Claudio Bombardelli, Mario Cosmo, Martin Harwit, David Leisawitz, Rodger Farley, Stephen Rinehart, David Quinn, David Miller, "Far-Infrared/Submillimeter Astronomical Interferometry with Spaceborne Tether Formations," Astrophys Space Sci (2006) 302:225–239 DOI 10.1007/s10509-006-9038-7

[4] Harwitt et al, "Submillimeter Probe of the Evolution of Cosmic Structure" SPECS (2005).

[5] S.Rinehart and the SPECS mission study team "SPECS: The Submillimetre Probe of the Evolution of Cosmic Structure." (2006)

[6] F.Helmich & R.Ivison "FIRI-A far-infrared interferometer"

[7] M.E.Wilson et al. "The Space Infrared Interferometric Telescope (SPIRIT): Optical System Design Considerations" (2007)

[8] Amato, M., Benford, D.J., Moseley, S.H., Roman, J. An engineering concept and enabling technologies for SAFIR, in: Mather, J.C. (Ed.), IR Space Telescopes and Instruments. Proc. SPIE, vol. 4850. SPIE – The International Society for Optical Engineering, Bellingham, WA, pp. 1120–1131, 2003.

[9] Blain, A. SCUBA deep fields and source confusion, in: Cristiani, S., Renzini, A., Williams, R.E. (Eds.), ESO/ECF/STScI Workshop Proc. Deep Fields. ESO Symp. Series, vol. xxvi. Springer, Berlin, pp. 129–134, 2000.

[10] Dragovan, M. DART system for far-IR/submillimeter membrane telescopes, in: MacEwen, H.A. (Ed.), Highly Innovative Space Telescope Concepts. Proc. SPIE, vol. 4849. SPIE – The International Society for Optical Engineering, Bellingham, WA, pp. 1–7, 2003.

[11] Evans II, N.J. Physical conditions in regions of star formation. Annu.Rev. Astr. Astrophys. 37, 311–362, 1999.

[12] Evans, N.J., II, Star and planet formation studies with new generation Infrared telescopes. BAAS, 33, 910, 2001. Available from <http://space.gsfc.nasa.gov/astro/aasbeyond/evans>.

[13] Farley, R.E., Quinn, D.A. Tethered formation configurations – meeting the scientific objectives of large aperture and interferometric science, in: Space 2001. American Institute of Aeronautics and Astronautics, Paper 2001-4770 (AIAA Accession number 39913), 2001.

[14] Haiman, Z., Rees, M.J., Loeb, A. H2 cooling of primordial gas triggered by UV irradiation. ApJ 467, 522–531, 1996.

[15] Kogut, A., Spergel, D.N., Barnes, C., Bennett, C.L., Halpern, M., Hinshaw, G., Jarosik, N., Limon, M., Meyer, S.S., Page, L., Tucker, G.S., Wollack, E., Wright, E.L. First year Wilkinson Microwave Anisotropy Probe (WMAP) observations: temperature polarization correlation. ApJS 148, 161–173, 2003.

[16] Leisawitz, D.T., Danchi, W.C., DiPirro, M.J., Feinberg, L.D., Gezari, D.Y., Hagopian, M., Langer, W.D., Mather, J.C., Moseley, S.H., Shao, M., Silverberg, R.F., Staguhn, J., Swain,

M.R., Yorke, H.W., Zhang, X. Scientific motivation and technology requirements for the SPIRIT and SPECS far-infrared/submillimeter space interferometers, in: Breckinridge, J.B., Jakobsen, P. (Eds.), UV, Optical, and IR Space Telescopes and Instruments. Proc. SPIE, vol. 4013. SPIE – The International Society for Optical Engineering, Bellingham, WA, pp. 36–46, 2000.

[17] Leisawitz, D., Armstrong, T., Benford, D., Blain, A., Borne K., Danchi, W., Evans, N., Gardner, J., Gezari, D., Harwit, M.,Kashlinsky, A., Langer, W., Lawrence, C., Lawson, P., Lester, D.,Mather, J., Moseley, S.H., Mundy, L., Rieke, G., Rinehart, S., Shao, M., Silverberg, R., Spergel, D., Staguhn, J., Swain, M., Traub, W., Unwin, S., Wright, E., Yorke, H., Probing the invisible universe: the case for far-IR/submillimeter interferometry, in: Benford, D.J., Leisawitz, D.T. (Eds.), Second Workshop on New Concepts for Far-Infrared and Submillimeter Space Astronomy, NASA CP-2003-212233. NASA, Washington, DC, pp. 166–176, 2003a. Available from <http://xxx.lanl.gov/abs/astro-ph/0202085>.

[18] Leisawitz, D., Benford, D.J., Kashlinsky, A., Lawrence, C.R., Mather, J.C., Moseley, S.H., Rinehart, S.A., Silverberg, R.F., Yorke, H.W. Prospecting for heavy elements with future far-IR/submillimeter observatories, in: Woodward, C. (Ed.), The Heavy Element Trail From Galaxies to Habitable Worlds. Astronomical Society of the Pacific, San Francisco, CA, 2003b (in press).

[19] Leisawitz, D., Frey, B.J., Leviton, D.B., Martino, A.J., Maynard, W.L., Mundy, L.G., Rinehart, S.A., Teng, S.H., Zhang, X. The Wide-Field Imaging Interferometry Testbed I: purpose, testbed design, data, and synthesis algorithms, in: Shao, M. (Ed.), Interferometry in Space, Proc. SPIE, vol. 4852, pp. 255–267, 2003c.

[20] Mariotti, J.-M., Ridgway, S.T. Double Fourier spatio-spectral interferometry – combining high spectral and high spatial resolution inthe near infrared. A&A 195, 350, 1988.

[21] Mather, J.C., Moseley, Jr., S.H., Leisawitz, D., Dwek, E., Hacking, P., Harwit, M., Mundy, L.G., Mushotzky, R.F., Neufeld, D., Spergel, D., Wright, E.L. The Submillimeter frontier: a space science imperative. Rev. Sci. Instr. (submitted). Available from <http://xxx.lanl.gov/abs/astro-ph/9812454>.

[22] Miller, D., Saenz-Otero, A., Wertz, J., Chen, A., Berkowski, G., Brodel, C., Carlson, S., Carpenter, D., Chen, S., Cheng, S., Feller, D., Jackson, S., Pitts, B., Perez, F., Szuminski, J., Sell, S. SPHERES: a testbed for long duration satellite formation flying in micro-gravity conditions, in: Proc. AAS/AIAA Space Flight Mechanics Meeting, Clearwater, FL, paper 00–110, 2002. Available from <http://ssl.mit.edu/spheres/library/AAS-AIAA.pdf>.

[23] Rupp et al, "AUTONOMOUS FORMATION FLYING AT DLR'S GERMAN SPACE OPERATIONS CENTER (GSOC)," 58TH INTERNATIONAL ASTRONAUTICAL CONGRESS, Hyderabad, India (2007)

[24] Delpech et al, "RESULTS OF PRISMA / FFIORD EXTENDED MISSION AND APPLICABILITY TO FUTURE FORMATION FLYING AND ACTIVE DEBRIS REMOVAL MISSIONS," 5th SFFMT, DLR, Munich, 2013

[25] Bainum, Peter M.; Harkness, Richard E.; Stuiver, Willem, "Attitude Stability and Damping of a Tethered Orbiting Interferometer Satellite System," Journal of Astronautical Sciences, Vol. 19, p.364 (1972)

[26] Decou, Anthony B., "Tether static shape for rotating multimass, multitether, spacecraft for 'triangle' Michelson interferometer," Journal of Guidance, Control, and Dynamics (ISSN 0731-5090), vol. 12, Mar.-Apr. 1989, p. 273-275. (1989).

[27] Bombardelli, Claudio; Lorenzini, Enrico C.; Quadrelli, Marco B., "Retargeting Dynamics of a Linear Tethered Interferometer," Journal of Guidance, Control, and Dynamics, vol. 27, issue 6, pp. 1061-1067 (2004).

[28] Kumar, K. D.; Yasaka, T., "Rotation Formation Flying of Three Satellites Using Tethers," Journal of Spacecraft and Rockets, vol. 41, issue 6, pp. 973-985 (2004)

[29] Lorenzini, 1987 and 1991

[30] Lorenzini, E. C., "Large Tether-Connected Two-Dimensional Structures in Low Earth Orbit," Proceedings of the Pacific Basin International Symposium on Advances in Space Science Technology and its Applications, pp. 792-800, 7-10 June 1987, Beijing, China, p.792 (1987).

[31] Lorenzini, E. C.; Carroll, J. A., "In-Orbit Experimentation with the Small Expendable-Tether Deployment System," Proceedings of the 41st Congress of the International Astronautical Federation, Dresden, Germany, 6-12 October 1990, Paper IAF-90-048, p.048 (1990).

[32] Lorenzini et al., Astrophys. Space Sci. (2006)

[33] Leisawitz et al, "The Space Infrared Interferometric Telescope (SPIRIT): A Far-IR Observatory for High-resolution Imaging and Spectroscopy," Decadal Survey White Paper (2010).

[34] Reinhart et al, "The Balloon Experimental Twin Telescope for Infrared Interferometry (BETTII): An Experiment for High Angular Resolution in the Far-Infrared," PASP (2014).

[35] ESA report, "FIRI, Far Infrared Interferometer," ESA CDF Study Report CDF-49(A) (2006).

[36] NASA web page, " International space station, facts and figures," http://www.nasa.gov/mission_pages/station/main/onthestation/facts_and_figures.html#.VNhsDBanZck.

[37] Tibert, G., "Deployable Tensegrity Structures for Space Applications" PhD Thesis, Kungl Tekniska Hogskolan, Stockholm, Sweden (2002).

[38] ROCCOR web page, "Roll-able Trusses", http://www.roccor.com/products/roll-able-trusses/

6 APPENDICES

In addition to the options for covering the u-v plane discussed in the report, we also performed a very preliminary study of an alternative concept, named SPIRO (through a similarity with its baseline tracks and a spirograph). While we do not feel this concept sufficiently mature to be taken into account in the trade-off, and having a certain number of open questions such as cooling of the periscope mirrors located in the joints, we still find the concept interesting and present it here as an appendix to the report.

6.1 SPIRO: NEW INTERCONNECTED INTERFEROMETER CONCEPT

In this section is reported a simulation concerning the dynamic motion of a new concept of interferometer with the two telescope connected to the central HUB by means of four booms, two of which, the ones connected to the telescopes, with capability to rotate independently of each other on the plane perpendicular to the ILS. The system appears to offer the possibility of a good coverage of the uv plane, without thrusters assist, while being placed in rotation under appropriate initial conditions
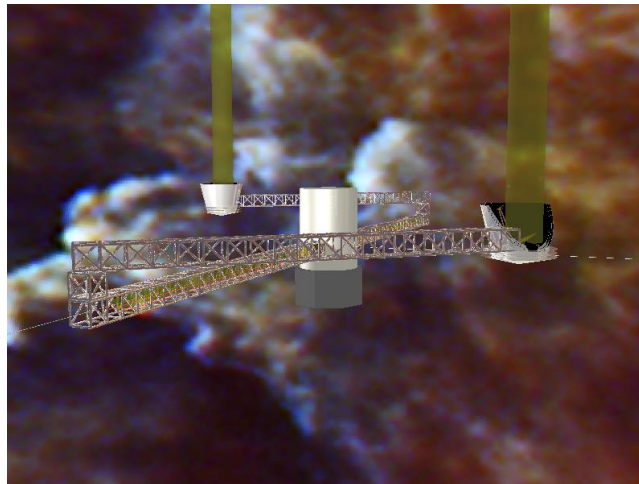
Figure 6.1-0 Simplistic rendering of the SPIRO concept with the double truss with periscope joints. The clear advantage of such a concept (which present other challenges) is the capability of changing the baselines without necessarily varying the beam-shape or optical coupling to the instrument. (as well as replacing linear motion with a rotating one)

6.1.1 Spiro - Dynamic Simulation

In the figure_6.1-1 is presented the scheme used to perform the presented simulation executed using SIMMECHANICS a tools of MATLAB.

Three masses, representing respectively the central HUB and the two satellites telescopes (SAT1 and SAT2), are connected between them by means of four booms, as shown in the figure_6-1-1, where the connections are constituted by means of pivots, taken as ideal in this simulation (without frictions). In the table_6.1-1 are indicated the respective values.

Table_6.1-1 *Values used in the simulation*

Hub (Kg)	350

SAT1 (kg)	1000
SAT2 (kg)	1000
Boom1 = Boom2 (m)	25
Boom3 = Boom4 (m)	23
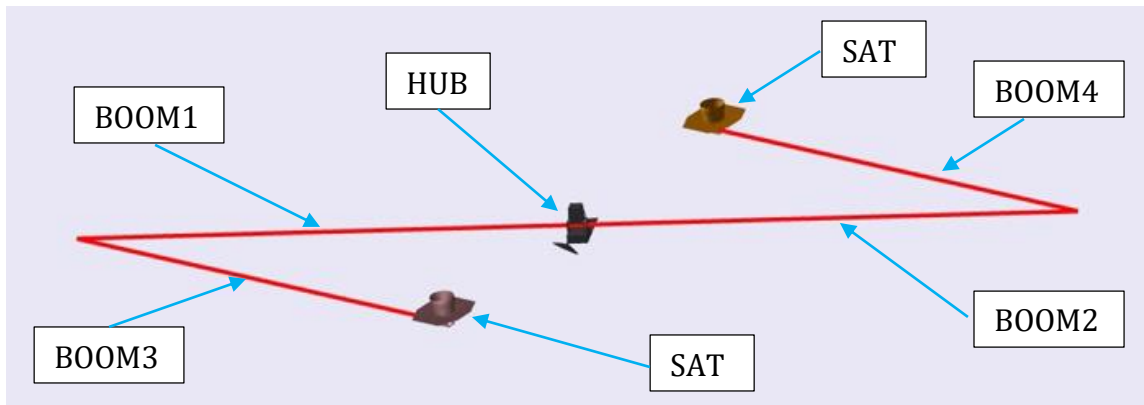
Figure_6.1-1 Scheme used to perform the SYMECHANIC simulation.

It is necessary to note that in these simulations, the boom1 and boom2 are rigidly connected and they can only rotate around their common pivot.

In the following the results of the simulation are shown obtained under different initial conditions given imposing different initial torques to the HUB and forces to the satellites, starting from the same steady initial interferometer condition, as illustrated in the following figure_2-2. Another condition is to maintain the tangential velocity not bigger that $1/26 \ ^m/_s$ during the successive interferometer dynamic.
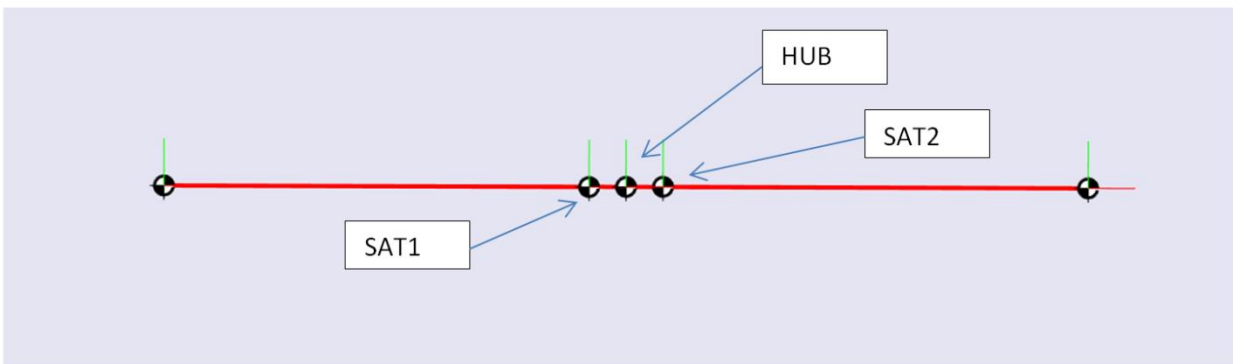
Figure_6.1-2 *Interferometer initial configuration.*

6.1.1.1 First Simulation – Action of the thrusters applied

In the following are reported the temporal evolution followed by the interferometer giving it an initial torque equal at $9Nm$ for $50s$ applied to the HUB, rigidly connected with the Boom1 and Boom2, torque direct perpendicular to the plane considerate, while the two thrusters acting on the two telescopes are kept turned off .
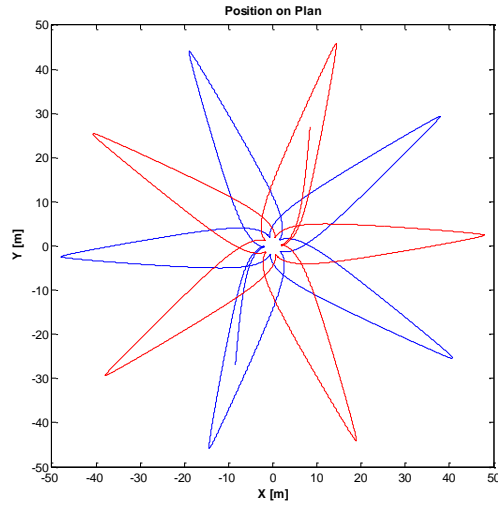
Figure_6.1.1-1 *Non thruster assisted trajectory followed by the two telescopes*
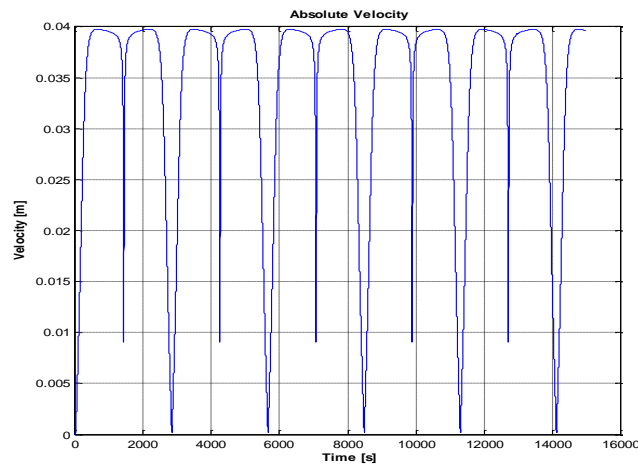
Figure_6.1.1-3 *Velocity of one of the two telescope vs time without thrusters assist*
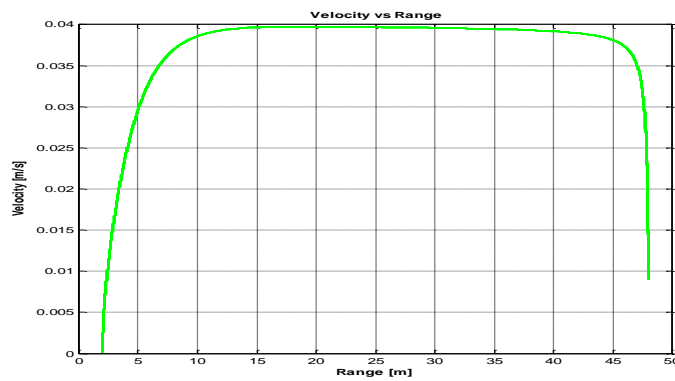
Figure_6.1.1-4 *Velocity of one of the two telescope vs range(or distance between each telescope and the central pivot) without thrusters assist*

From the last figure it is possible to see that for distances between 10 and 46m, the velocity is equal to $\frac{1}{26}$ m/s (as imposed by the initial conditions), while between 2 and 10m and between 50 and 46m the velocity is quite less than $\frac{1}{26}$ m/s, determining an increase of the observation time.

6.1.1.2 Second Simulation

In this simulation the torque on the central Hub has been kept to zero, while the two thrusters applied to the two telescopes, forces in opposite directions and perpendicular to the respective boom3 and boom4 equal to $12 \cdot 10^{-3}$ N for a time of $1000s$
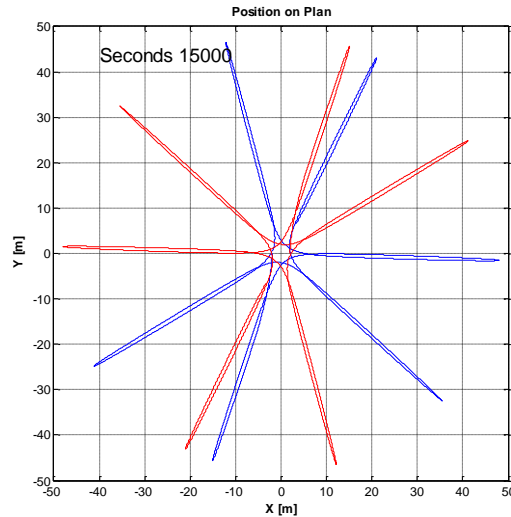
Figure_6.1.2-1 *Non thruster assisted trajectory followed by the two telescopes*
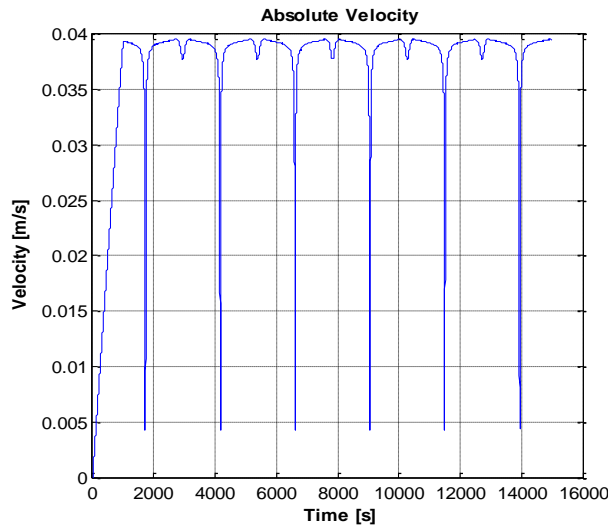
Figure_6.1.1-3 *Velocity of one of the two telescope vs time without thrusters assist*
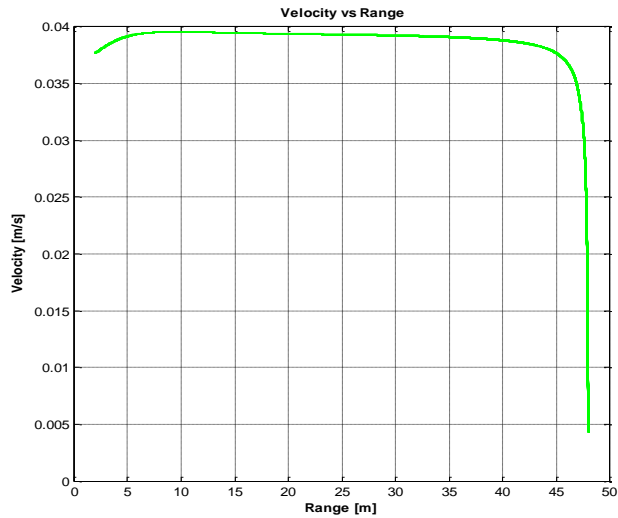
Figure_6.1.2-4 *Velocity of one of the two telescope vs range(or distance between each telescope and the central pivot) without thrusters assist*

In this case the coverage is not good because the two satellites tend to repass on the same zone.

6.1.1.3 Third Simulation

In this simulation a central torque equal to $-13.5 \, N \cdot m$ is applied for $1000 \, s$, and controlled the temporal evolution during $24h$.
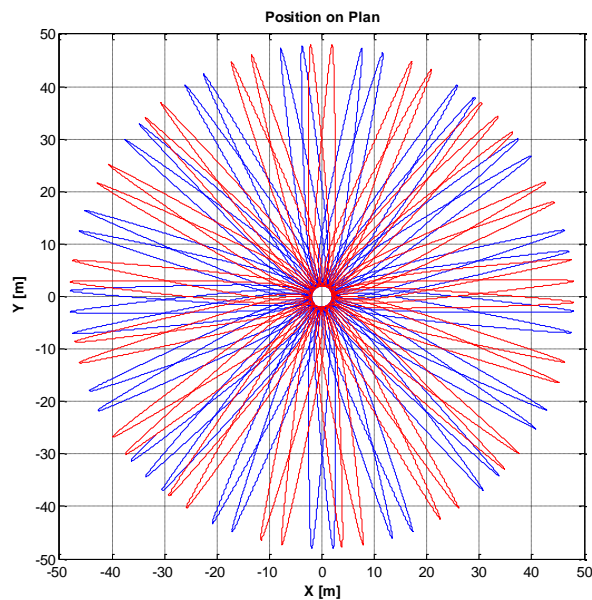
Figure_6.1.3-1 *Non thruster assisted trajectory followed by the two telescopes*
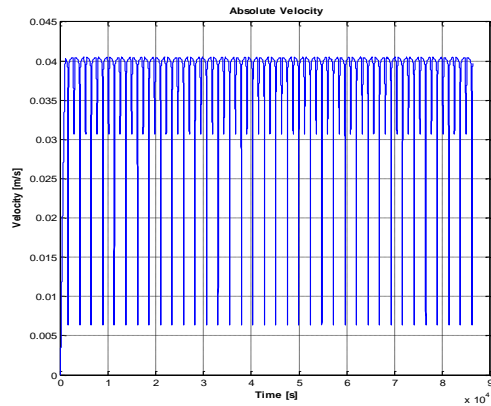
Figure_6.1.3-3 *Velocity of one of the two telescope vs time without thrusters assist*
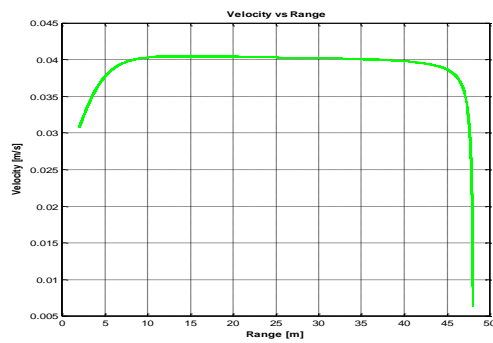
Figure_6.1.3-4 *Velocity of one of the two telescope vs range(or distance between each telescope and the central pivot) without thrusters assist*

For this simulation, in the following figures we show the temporal evolutions followed by the two satellites.